Inorganic Chemistry

Article

pubs.acs.org/IC

Tuning Ligand Effects and Probing the Inner-Workings of Bond Activation Steps: Generation of Ruthenium Complexes with Tailor-Made Properties

Fritz Weisser,[†] Sebastian Plebst,[‡] Stephan Hohloch,[†] Margarethe van der Meer,[†] Sinja Manck,[†] Felix Führer,[†] Vanessa Radtke,[†] Daniel Leichnitz,[†] and Biprajit Sarkar*[,†]

[†]Institut für Chemie und Biochemie, Anorganische Chemie, Freie Universität Berlin, Fabeckstraße 34-36, D-14195 Berlin, Germany

[‡]Institut für Anorganische Chemie, Universität Stuttgart, Pfaffenwaldring 55, D-70569 Stuttgart, Germany

Supporting Information

ABSTRACT: Activating chemical bonds through external triggers and understanding the underlying mechanism are at the heart of developing molecules with catalytic and switchable functions. Thermal, photochemical, and electrochemical bond activation pathways are useful for many chemical reactions. In this Article, a series of Ru^{II} complexes containing a bidentate and a tripodal ligand were synthesized. Starting from all-pyridine complex $\mathbf{1}^{2+}$, the pyridines were stepwise substituted with "click" triazoles ($\mathbf{2}^{2+}$–$\mathbf{7}^{2+}$). Whereas the thermo- and photoreactivity of $\mathbf{1}^{2+}$ are due to steric repulsion within the equatorial plane of the complex, $\mathbf{3}^{2+}$–$\mathbf{6}^{2+}$ are reactive because of triazoles in axial positions, and $\mathbf{4}^{2+}$ shows unprecedented photoreactivity. Complexes that feature neither steric interactions nor axial triazoles ($\mathbf{2}^{2+}$ and $\mathbf{7}^{2+}$) do not show any reactivity. Furthermore, a redox-triggered conversion mechanism was discovered in $\mathbf{1}^{2+}$, $\mathbf{3}^{2+}$, and $\mathbf{4}^{2+}$. We show here ligand design principles required to convert a completely inert molecule to a reactive one and vice versa, and provide mechanistic insights into their functioning. The results presented here will likely have consequences for developing a future generation of catalysts, sensors, and molecular switches.

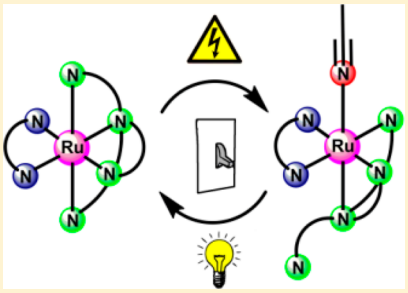

INTRODUCTION

Ru–polypyridine complexes have attracted considerable attention in the field of coordination chemistry in the past two decades.[1−6] They have found numerous applications, for example, as photosensitizers in the famous Grätzel cell[1] or in various photocatalytic redox reactions.[2] Furthermore, they have been used to study optoelectronics[3] and magnetism[4] and to catalyze oxygenation reactions[5] or water oxidation.[6] The complex $[Ru(TPA)(bpy)]^{2+}$ [$\mathbf{1}^{2+}$, Scheme 1, TPA = tris(2-methylpyridine)amine] is another interesting polypyridine complex. Apart from biochemical applications, such as DNA intercalation[7a] and NAD^+ regeneration,[7b] it was studied as a molecular switch.[7c−f]

Triggered by light or heat, one of the three pyridine arms of TPA in $\mathbf{1}^{2+}$ dissociates.[7c] The vacant coordination site can be filled by a solvent molecule or an anion. In addition, a high-valent Ru^{IV}=O species was generated from $\mathbf{1}^{2+}$, where an oxido ligand occupies the sixth coordination site,[7d,e] and the Ru^{IV} oxido species can transfer its O atom to an organic substrate. Variations of this system were mainly focused on the nature of the bidentate ligand and on maximizing the thermal reactivity.[7c] Previously, we showed that substitution of the pyridine rings in TPA by triazoles has drastic effects on the photo-, thermo-, and redox-reactivity of the corresponding Ru(II)–DMSO complexes.[8a] We therefore employed this strategy for the fine-tuning of complex $\mathbf{1}^{2+}$. Metal complexes of tripodal triazole ligands are useful for a variety of catalytic and switchable functions.[8] Here, we present a series of complexes ($\mathbf{1}^{2+}$–$\mathbf{7}^{2+}$, Scheme 1), in which the pyridines of $\mathbf{1}^{2+}$ are successively substituted by triazoles. Using various spectroscopic methods, we studied the effects of this substitution on the reactivity of the complexes.

RESULTS AND DISCUSSION

Synthesis and ^{1}H NMR Spectroscopy. The complexes were synthesized in a two-step process. First, the precursor $Ru(DMSO)_4Cl_2$ was allowed to react with the bidentate ligand.[9] The resulting intermediates were heated in ethylene glycol with tripodal ligands to afford complexes $\mathbf{1}(PF_6)_2$–$\mathbf{7}(PF_6)_2$ in good yields (Supporting Information Scheme S5). As an example for the structural evaluation of the ^{1}H NMR data, the spectrum of $\mathbf{5}^{2+}$ in acetone-d_6 is discussed here in detail (Figure 1). The spectrum shows one set of pyridine signals (labeled a in Figure 1), that is, two doublets (at 10.59 and 8.28 ppm) and two doublets of doublets (at 8.17 and 7.79 ppm). Hence, only one of two possible isomers is formed. This could be due to either the trans effect between the σ-donating central amine and the π-accepting pyridine or the C–H···N interaction between pyridine and triazole in the equatorial plane (vide infra). There are three singlets at 9.07, 8.13, and 8.07 ppm, which integrate for 1 proton, 2 protons, and 1 proton, respectively, and can be assigned to the H atoms on the

Received: November 23, 2014
Published: May 6, 2015

DOI: 10.1021/ic502807d
Inorg. Chem. 2015, 54, 4621−4635

Scheme 1. Complexes 1^{2+}–7^{2+}[a]

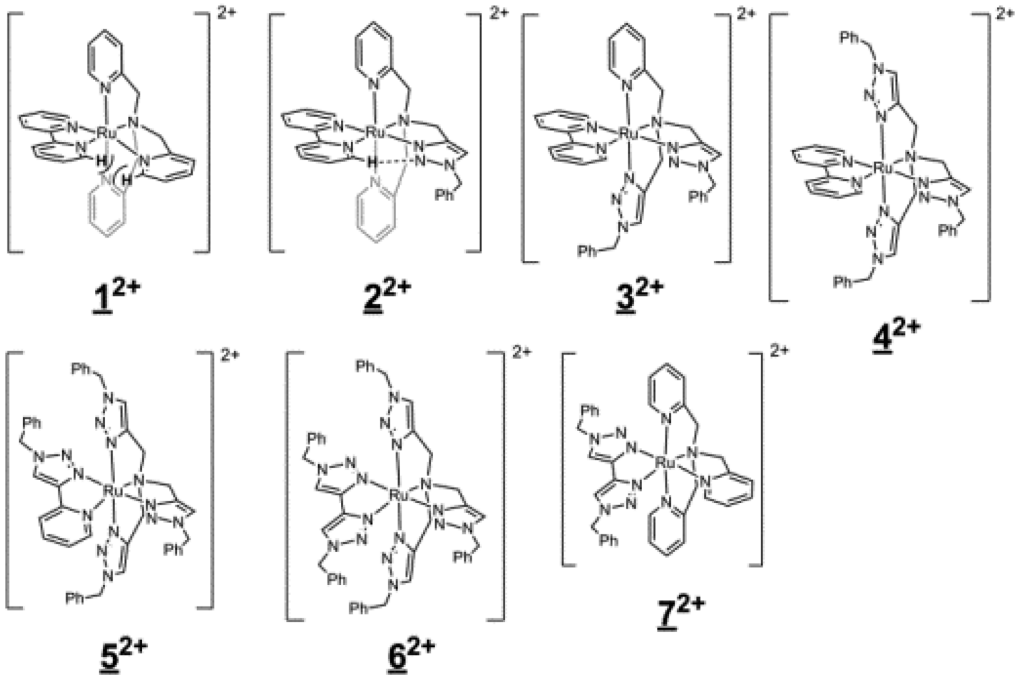

[a]Each complex has two PF_6^- counterions.

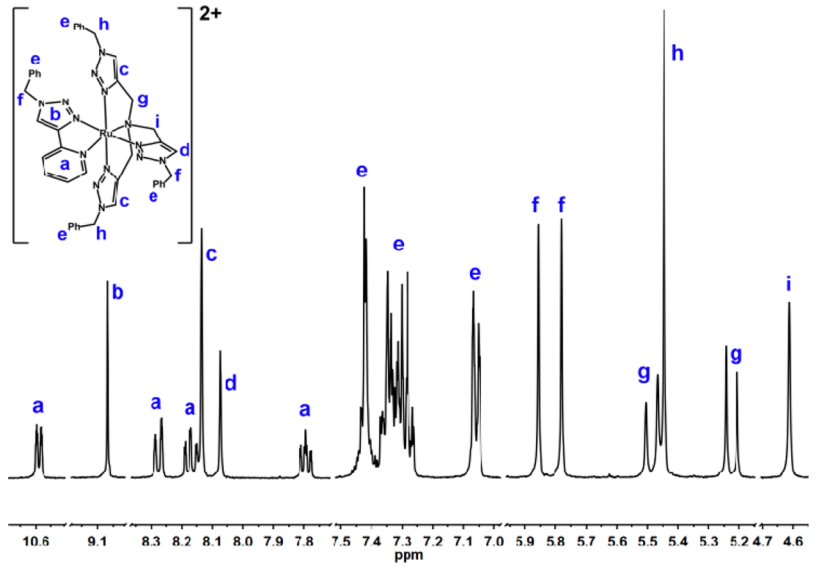

Figure 1. ^{1}H NMR spectrum of complex $\mathbf{5}^{2+}$ recorded in acetone-d_6. Parts of the spectrum are cut for better visibility of the signals.

triazole rings (Figure 1, signals b, c, and d). Therefore, there are two identical triazole arms of the tripodal ligand in the axial positions trans to each other.

Between 6 and 4 ppm, the resonances of the CH_2 groups from the two ligands are seen. The benzylic CH_2 groups of the residues on the triazoles show signals at 5.86, 5.78, and 5.45 ppm, which integrate for 2, 2, and 4 protons, respectively (Figure 1, signals f and h). For the two axial arms, the CH_2 protons between the triazoles and the central amine have different chemical environments. This results in geminal coupling and the appearance of two pseudodoublets at 5.49 and 5.22 ppm, both of which integrate for 2 protons (Figure 1, signals g). The triazole–CH_2–N_{amine} group in the equatorial position lies in a mirror plane of the molecule and therefore shows a singlet, which integrates for 2 protons (Figure 1, signal i).

Similarly, the ^{1}H NMR spectrum of $\mathbf{2}^{2+}$ (Figure 2) reveals the symmetric geometry of the complex, because there is one set of pyridine signals with double intensity, which can be assigned to the two axial pyridine arms. Furthermore, the CH_2 resonances of $\mathbf{2}^{2+}$ show 2 pseudodoublets and 2 singlets, which is only possible if the CH_2 groups of the triazole arm are in the mirror plan of the molecule. The unsymmetric geometry of $\mathbf{3}^{2+}$ is obvious from the two singlets at 8.12 and 8.08 ppm (in acetone-d_6, Supporting Information Figure S7), which are assigned to two triazole rings in different positions (axial and equatorial). In addition, the unsymmetric nature of $\mathbf{3}^{2+}$ results in enhanced geminal coupling of the CH_2 protons.

DOI: 10.1021/ic502807d
Inorg. Chem. 2015, 54, 4621–4635

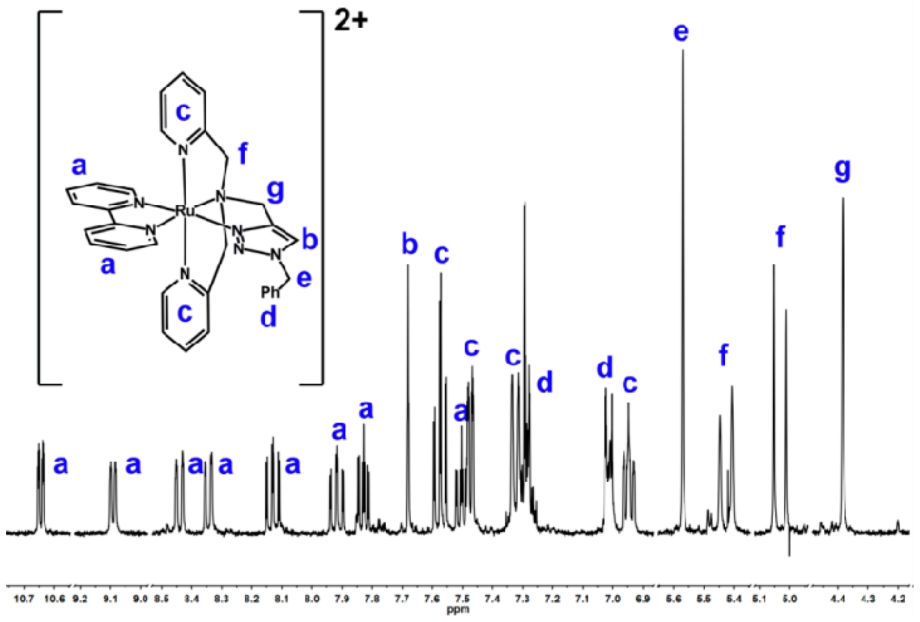

Figure 2. ^{1}H NMR spectrum of complex $\mathbf{2}^{2+}$ recorded in CD_3CN. Parts of the spectrum are cut for better visibility of the signals.

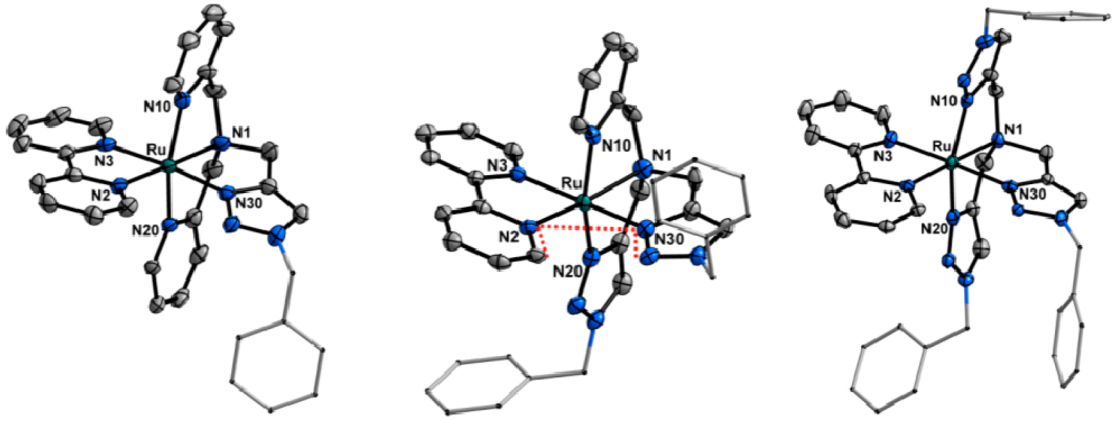

Figure 3. Perspective view of $\mathbf{2}^{2+}$ (left), $\mathbf{3}^{2+}$ (middle), and $\mathbf{4}^{2+}$ (right): thermal ellipsoids are drawn at the 50% probability level, and benzyl moieties are drawn as stick models for better visibility. H atoms, counterions, and solvent molecules are omitted for clarity. The red dotted line indicates the torsion angle between the equatorial arm and bpy.

Crystal Structure Analyses. For $\mathbf{1}^{2+}$–$\mathbf{4}^{2+}$ and $\mathbf{7}^{2+}$, we were able to obtain single crystals suitable for X-ray diffraction analyses, and the geometry from the solid-state structures matches the ^{1}H NMR analyses in solution. In all complexes with bipyridine as a bidentate ligand, the N_{bpy}–Ru bond opposite to the central amine nitrogen atom is shorter [2.058(4)–2.068(2) Å] than the N_{bpy}–Ru bond opposite to the equatorial arm [2.090(4)–2.110(2) Å]. This is due to a trans influence between the π-accepting pyridine and the σ-donating amine nitrogen atom. In **7**, where the bidentate ligand is a bis-1,2,3-triazole, both $N_{triazole}$–Ru distances are the same [2.072(5) Å], which points to the absence of a trans influence. This can be explained by the much weaker π-accepting character of the triazole moiety compared to that of a pyridine.

The most remarkable changes in the molecular structure are due to the substitution of the equatorial pyridine arm of TPA in $\mathbf{1}^{2+}$ by a triazole (in $\mathbf{2}^{2+}$–$\mathbf{4}^{2+}$). Whereas N30–Ru is the longest of all six N–Ru distances in $\mathbf{1}^{2+}$ [2.102(3) Å], it becomes the shortest N–Ru distance in $\mathbf{2}^{2+}$ [2.041(4) Å] and increases only slightly upon further substitution of pyridine arms [2.052(2) and 2.054(2) Å in $\mathbf{4}^{2+}$]. At the same time, the torsion angle between the equatorial N-heterocyclic arm and bpy (torsion angle indicated by dotted lines in Figure 3) decreases from 42.9° in $\mathbf{1}^{2+}$ to 15.5° in $\mathbf{2}^{2+}$ to 0.4 in $\mathbf{3}^{2+}$ and $\mathbf{4}^{2+}$.

In $\mathbf{1}^{2+}$, there is steric repulsion between the C–H bonds of a pyridine from the equatorial TPA arm and one from bpy. In fact, Kojima et al. suggested that this steric interaction is one of the main reasons for the reactivity of $\mathbf{1}^{2+}$.[7c] In complexes $\mathbf{2}^{2+}$–$\mathbf{4}^{2+}$, there is no such steric repulsion. Instead, there are short C–H···N interactions (dotted line for $\mathbf{2}^{2+}$ in Scheme 1) between bpy and the N atom of the equatorial triazole ring [2.255(4)–2.294(2) Å]. Hence, by exchanging the equatorial pyridine arm of TPA with a triazole, the strong repulsion between a pyridine arm and bipyridine ligand is turned into a weak attraction. This finding is corroborated by the structure of $\mathbf{7}^{2+}$. Here, it is not the pyridine moiety of the equatorial arm but those of the bidentate ligand that are substituted by triazoles. However, the result is the same. Instead of steric repulsion, there is a short N_{eq}–Ru distance [2.055(5) Å], a short C–H··· N distance [2.395(6) Å], and a small torsion angle (12.1°). For

DOI: 10.1021/ic502807d
Inorg. Chem. 2015, 54, 4621–4635

5^{2+} the diffraction data set was not good enough to derive exact bond parameters. However, the connectivity (Supporting Information Figure S30) showed that the complex forms the isomer shown in Scheme 1. Supporting Information Table S1 summarizes the important bond lengths and angles for the complexes.

Cyclic Voltammetry. The electrochemical properties of complexes 1^{2+}–7^{2+} were investigated by cyclic voltammetry (CV). In DCM, all complexes show one reversible metal-centered oxidation process. The oxidation potential remains unaffected by the substitution of pyridine rings (Table 1).

Table 1. Redox Potentials of the Complexes 1^{2+}–7^{2+} Measured at 100 mV/s with 0.1 M Bu_4NPF_6 and Referenced versus the Ferrocene/Ferrocenium Couple

complex	ox. in DCM [V] (peak separation [mV])	ox. in CH_3CN [V] (peak separation [mV])	red. in CH_3CN [V] (peak separation [mV])
1^{2+}	0.75 (81)	0.71;[a] 0.94[a]	−1.83 (75)
2^{2+}	0.75 (76)	0.69 (69)	−1.86 (75)
3^{2+}	0.76 (85)	0.70;[a] 0.87[a]	−1.88 (68)
4^{2+}	0.76 (85)	0.72;[a] 0.85[a]	−1.89 (66)
5^{2+}	0.76 (92)	0.77 (65)	−2.36[a]
6^{2+}	0.76 (118)	0.76 (70)	−2.59[a]
7^{2+}	0.76 (103)	0.72 (70)	−2.40[a]

[a]Peak potentials of the forward processes are given.

When measured in CH_3CN, the bpy-containing complexes (1^{2+}–4^{2+}) show reversible reduction processes, which become irreversible when pyridines of the bidentate ligand are substituted (5^{2+}–7^{2+}). In CH_3CN, the oxidation of 1^{2+}, 3^{2+}, and 4^{2+} leads to the formation of the corresponding acetonitrile adducts; instead of one reversible oxidation, two irreversible processes are observed, and the mechanism of this redox-triggered transformation is explained in more detail below.

The reduction slightly shifts to more negative potentials with an increasing number of triazoles in the tripodal ligand (1^{2+}–4^{2+}). Upon pyridine substitution in the bidentate ligand (5^{2+}–7^{2+}), the irreversible reductions shift drastically to more negative potentials (Table 1). Hence, the reduction is a one-electron process centered on the bidentate ligand. This is corroborated by EPR spectra of the reduced species 1^{+}–4^{+}. The spectra show isotropic signals with hyperfine coupling to two ^{14}N nuclei. Supporting Information Figure S56 shows the experimental and simulated EPR spectra of 2^{+}.

When the pyridine rings of the bidentate ligand are substituted with triazoles, the ligand becomes harder to reduce, which is due to the weaker accepting character of the triazole compared to that of pyridine. On the other hand, when the pyridine rings of the tripodal ligand are substituted with weaker accepting triazoles, the electron density at the Ru center should increase. However, this is not reflected in the oxidation potential of complexes 1^{2+}–4^{2+}. There are two possible explanations for this observation: In addition to being weaker π-acceptors, it has also been reported that 1,2,3-triazoles are weaker σ-donors and less basic than pyridines.[10] Hence, the less accepting and less donating character of the triazole could cancel out and leave the Ru^{II}/Ru^{III} unchanged. However, for Ru^{II}–DMSO complexes, the stepwise substitution of triazoles for pyridines leads to a slight decrease in the oxidation potential and to an increase in back bonding to the DMSO ligand.[8a] If the triazole-for-pyridine substitution leads to an increase in electron density at the metal center, this could be compensated by increased back-donation to the bpy ligand, which would leave the oxidation potential unchanged. Indeed, bpy becomes harder to reduce going from 1^{2+} to 4^{2+}, and the reduction potential of 6^{2+} is 0.2 V more negative than that of 7^{2+}.

UV–Vis Spectroelectrochemistry. The UV–vis absorption spectra (Figure 4 and Supporting Information Figure S45

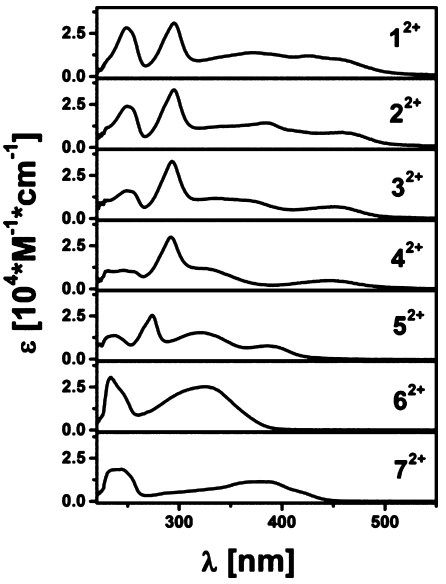

Figure 4. UV–vis spectra of the complexes 1^{2+}–7^{2+} recorded in DCM.

and Table S5) can be explained by combining the spectral properties of the two fragments {Ru–bident}[11] and {Ru–tripod}.[8a] The bpy-containing complexes 1^{2+}–4^{2+} all show an intense band at approximately 295 nm, which can be assigned to a π–π^* transition in the bpy ligand and metal-to-ligand-charge-transfer (MLCT) transitions. There is a weaker band at around 450 nm, which can be assigned to a MLCT transition from the d orbitals of Ru to the π^* orbital of bpy. This assignment is based on a comparison with the absorption spectra of $[Ru(bpy)_3]^{2+}$[11a] and $[Ru(bpy)(CH_3CN)_4]^{2+}$.[11b]

On the basis of a comparison with complexes of the formula $[Ru(L)(DMSO)(Cl)]PF_6$,[8a] we assign the bands between 300 and 450 nm to MLCT transitions within the fragment {Ru–tripod}. Upon substitution of the pyridine rings with triazoles, the {Ru–tripod} MLCT bands shift to shorter wavelengths, because the acceptor orbitals of the tripodal ligand increase in energy. Furthermore, 1^{2+} shows an intense band at around 250 nm, which can be assigned to π–π^* transitions in the pyridine moieties of the tripodal ligand. Consequently, upon stepwise substitution of the pyridine rings in 2^{2+}, 3^{2+}, and 4^{2+}, this band gradually disappears.

Analogous to the {Ru–tripod} MLCT transitions, all bands assigned to the {Ru–bident} fragment shift to shorter wavelengths (higher energies) upon substitution of the pyridine rings in the bidentate ligand. For example, the π–π^* transition of the bidentate ligand is shifted from 292 nm in 4^{2+} to 274 nm in 5^{2+} to 234 nm in 6^{2+}. The MLCT band seen for 1^{2+}–4^{2+} around 450 nm corresponds to a Ru($d\pi$)–bpy(π^*) transition. Because the oxidation process observed in CV is metal-centered and the reduction process is bpy-centered (vide supra), the energy of this MLCT band correlates with the potential difference between oxidation and reduction in the CV. As the

DOI: 10.1021/ic502807d
Inorg. Chem. 2015, 54, 4621–4635

reduction potential becomes more negative from 4^{2+} to 6^{2+}, the HOMO−LUMO gap increases, and the MLCT band is blue-shifted from 450 to approximately 350 nm.

Upon oxidation of all complexes, the bands assigned to MLCT transitions disappear, and the oxidized species show mostly bands at wavelengths shorter than 350 nm, which we assign to intraligand transitions (Figure 5). However, the

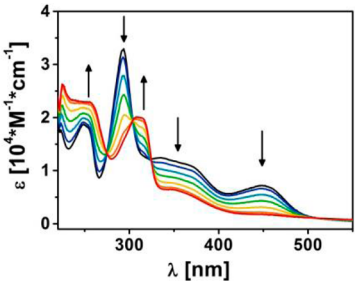

Figure 5. Changes in the UV−vis spectrum of 3^{2+} observed upon oxidation in DCM.

oxidized complexes 5^{3+}, 6^{3+}, and 7^{3+}, which have more electron-rich bidentate ligands, show weak bands in the range 350−600 nm, which we assign to LMCT transitions. The spectral changes agree well with a metal-centered oxidation resulting in decreased electron density at the Ru^{III} center.

The one-electron-reduced species 1^{+}−4^{+} show spectral signatures that are very similar to those of reduced $[Ru(bpy)_3]^{2+}$.[11a] They exhibit intense bands around 360 nm, which can be assigned to MLCT transitions, weaker bands between 400 and 600 nm, which can be assigned to π−π^* transitions in the reduced $bpy^{\bullet-}$ ligand, and very weak bands in the range 700−1100 nm, which we assign to an intraligand charge-transfer (ILCT) of reduced $bpy^{\bullet-}$ (Figure 6).[11a]

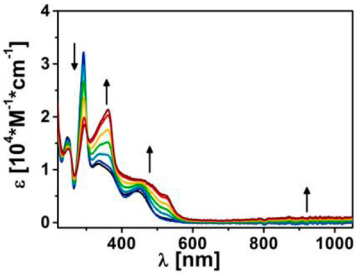

Figure 6. Changes in the UV−vis spectrum of 3^{2+} observed upon reduction in CH_3CN.

Thermo- and Photoreactivity. Complex 1^{2+} reacts in CD_3CN to form complex $[1(CD_3CN)]^{2+}$ (Figure 7),[7c] in which one of the TPA arms is replaced by a solvent molecule, and the TPA reorganizes its coordination mode relative to bpy (Scheme 2). This reaction can be triggered by heat (80 °C) or light (350−400 nm), and the structure of $[1(CH_3CN)]^{2+}$ has been determined before by X-ray diffraction analysis.[7d] We monitored the thermo- and photoreactivities of complexes 1^{2+}−7^{2+} with ^1H NMR spectroscopy. After being heated in CD_3CN for 2 days, 1^{2+}, 3^{2+}, and 4^{2+} had reacted and formed the corresponding CD_3CN adducts in 95%, 83%, and 55% yield, respectively. Complexes 2^{2+} and 5^{2+}−7^{2+} did not react.

It has been shown before that Ru^{II} complexes of 1,2,3- and 1,2,4-triazoles are susceptible to light-driven substitution and isomerization reactions.[12,13] When the samples were irradiated at 350−400 nm, a region where the MLCT transitions of the complexes are excited, a reactivity pattern different from that of the thermal reactions was observed (Figure 8). For 1^{2+}, a photoconversion efficiency of 53% $[1(CD_3CN)]^{2+}$ was obtained after 10 h. Whereas 2^{2+} did not react at all, $[3(CD_3CN)]^{2+}$ was obtained with 87% conversion efficiency after 15 h. Complex 4^{2+} is the most reactive complex under irradiation conditions, and $[4(CD_3CN)]^{2+}$ could be obtained with 99% photoconversion efficiency after 4 h, which is unprecedented for derivatives of 1^{2+}.[7c,f]

The reaction mixtures resulting from the irradiation of 3^{2+}−6^{2+} in CD_3CN were all submitted to mass spectrometry. The samples were first diluted with CH_3CN; hence, any acetonitrile species formed in the spectrometer should contain non-deuterated CH_3CN. The MS signatures for $[3(CD_3CN)]^{2+}$−$[6(CD_3CN)]^{2+}$ were found (Supporting Information Figures S6 and S7), which shows that acetonitrile adducts are formed during the photoreaction in CD_3CN. ^1H NMR data show that $[3(CD_3CN)]^{2+}$ and $[4(CD_3CN)]^{2+}$ have structures similar to that of $[1(CD_3CN)]^{2+}$,[7d] and $[3(CD_3CN)]^{2+}$ has a free triazole arm (Supporting Information Scheme S3). Upon the transformation of 1^{2+} to $[1(CD_3CN)]^{2+}$, there are two major changes observed in the ^1H NMR spectrum (Figure 7). First, whereas the two pyridine rings of the bpy ligand have different environments in 1^{2+}, they are identical in $[1(CD_3CN)]^{2+}$. As a result, the number of pyridine resonances decreases, and some of the bpy resonances are shifted to higher field. Second, the CH_2 resonances of the tripodal ligand are also shifted to higher field in $[1(CD_3CN)]^{2+}$. Whereas the singlet of the equatorial pyridine arm in 1^{2+} appears at 4.64 ppm, the singlet of the uncoordinated, free pyridine arm in $[1(CD_3CN)]^{2+}$ appears at 3.20 ppm (in CD_3CN).

Analogously to $[1(CD_3CN)]^{2+}$, both the bpy and CH_2 resonances of $[3(CD_3CN)]^{2+}$ are shifted drastically to higher field (Figure 9). Whereas the most low-field-shifted resonance of 3^{2+} appears at 10.64 ppm, the most low-field-shifted resonance of $[3(CD_3CN)]^{2+}$ appears at 8.86 ppm (Figure 9). The most high-field-shifted resonance of 3^{2+} appears at 4.25 ppm, whereas that of $[3(CD_3CN)]^{2+}$ appears at 3.15 ppm (Figure 9, signal j), which is close to the value of the free tripod arm in $[1(CD_3CN)]^{2+}$ (3.20 ppm). Because there are two singlets at 7.72 and 7.65 ppm (Figure 9, signals c and d) from two different triazoles, the free tripod arm of $[3(CD_3CN)]^{2+}$ must be a triazole arm, which renders the complex unsymmetrical.

Analogously, the structure of $[4(CD_3CN)]^{2+}$ is evidenced by its ^1H NMR spectrum (Figure 10). There is only one set of pyridine signals (Figure 10, signals a), which means that there is a mirror plane between the two bpy halfs. The two different triazole resonances with an integral ratio of 2:1 (Figure 10, signals b and c) point to an uncoordinated tripod arm. The CH_2 singlet at 3.16 ppm (Figure 10, signal h) and the two pseudodoublets at 4.12 and 3.66 ppm (Figure 10, signals g) indicate that the uncoordinated arm is in the mirror plane, and the coordinated arms are not in the mirror plane. For the molecule to be symmetrical, the central amine and the acetonitrile ligand must be in the mirror plane as well. All these geometrical requirements are met by the structure shown in Figure 10, which is analogous to the crystal structure found for $[1(CH_3CN)]^{2+}$.[7d]

There is a very different picture for the light-driven transformation of 6^{2+} to $[6(CD_3CN)]^{2+}$. The ^1H NMR

DOI: 10.1021/ic502807d
Inorg. Chem. 2015, 54, 4621−4635

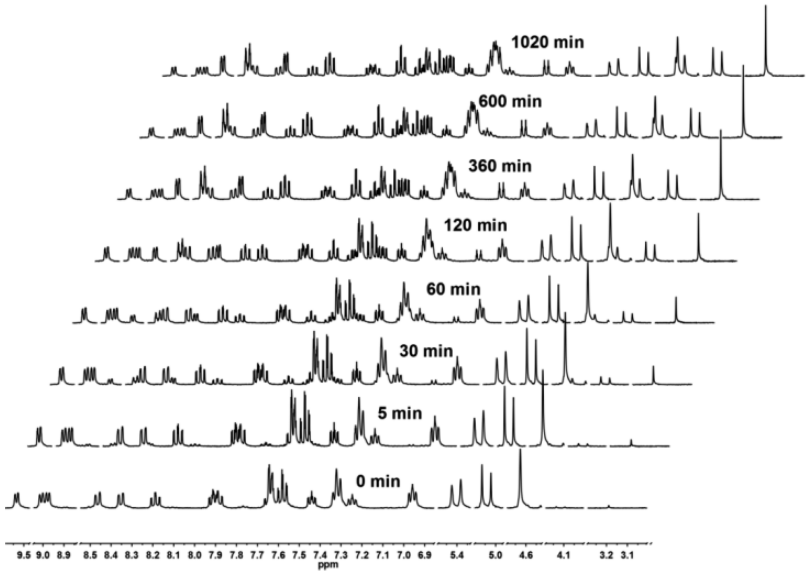

Figure 7. Changes in the ^{1}H NMR spectrum of $\mathbf{1}^{2+}$, observed upon irradiation at 350−400 nm.

Scheme 2. Thermo- and Photoreactivity of $\mathbf{1}^{2+}$

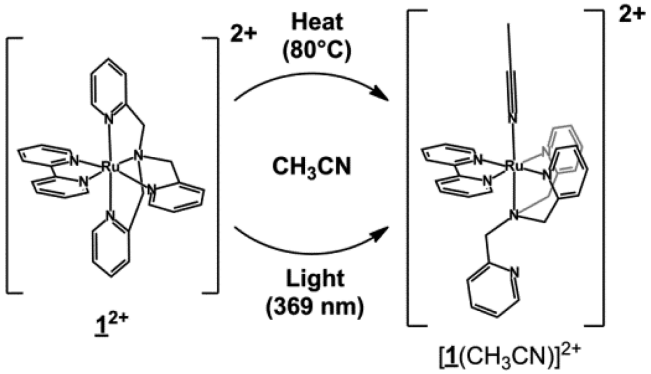

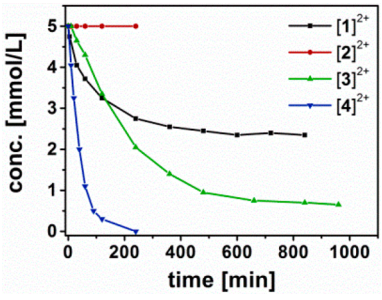

Figure 8. Change in concentration of $\mathbf{X}^{2+}$ over time upon irradiation (350−400 nm) in CD_3CN.

spectrum that results from the irradiation of $\mathbf{6}^{2+}$ in CD_3CN exhibits resonances of two species $[\mathbf{6a}(CD_3CN)]^{2+}$ and $[\mathbf{6b}(CD_3CN)]^{2+}$ in a ratio of 4:1 (Figure 11). The number of signals for $[\mathbf{6b}(CD_3CN)]^{2+}$ point to a symmetrical structure, and the chemical shifts of the triazole and CH_2 signals are almost identical to those of $[\mathbf{4}(CD_3CN)]^{2+}$. However, the major species $[\mathbf{6a}(CD_3CN)]^{2+}$ shows 5 different triazole singlets and a large number of CH_2 pseudodoublets. This indicates a highly unsymmetrical structure. Kojima et al. suggested a 7-coordinate intermediate for the photochemical reaction.[7c] Although a 7-coordinate structure could explain the ^{1}H NMR spectrum of $[\mathbf{6a}(CD_3CN)]^{2+}$, it is unlikely that such a structure would be stable enough to be detected by NMR spectroscopy. Only a few 7-coordinate Ru complexes have been reported, and they feature higher-valent Ru centers and smaller O donor ligands.[14] DFT calculations support a 6-coordinate structure of $[\mathbf{6a}(CD_3CN)]^{2+}$, as shown in Scheme 3. Starting from an optimized geometry of $\mathbf{6}^{2+}$ (Supporting Information Figure S79 and Table S7; modeled from the crystal structures of $\mathbf{4}^{2+}$ and $\mathbf{7}^{2+}$), we tried to optimize the geometry of both a 6-coordinate as well as a 7-coordinate unsymmetrical acetonitrile species (i.e., all 5 triazoles are different). Whereas the geometry of the 6-coordinate structure converged to a local minimum (Supporting Information Figure S80 and Table S8), a calculation starting from a 7-coordinate model led to an optimized geometry in which the acetonitrile molecule is no longer coordinated to the Ru center.

As mentioned above, the transformation of $\mathbf{X}^{2+}$ to $[\mathbf{X}(CD_3CN)]^{2+}$ requires both the substitution of a tripod arm by CD_3CN as well as the subsequent coordinative reorganization of the tripodal ligand. Hence, $[\mathbf{6a}(CD_3CN)]^{2+}$ could be the intermediate product of the ligand substitution, and its coordinative reorganization would lead to the formation of $[\mathbf{6b}(CD_3CN)]^{2+}$ (Scheme 3). The decoordination of an axial triazole arm also agrees well with the results of our mechanistic studies described below. For $[\mathbf{5}(CD_3CN)]^{2+}$, the chemical shifts in the ^{1}H NMR spectrum are similar to those of $[\mathbf{6a}(CD_3CN)]^{2+}$ (Supporting Information Figure S17).

When the complexes $\mathbf{1}^{2+}$ and $\mathbf{3}^{2+}$−$\mathbf{6}^{2+}$ are irradiated in NMR tubes in the range 350−400 nm, the formation of the acetonitrile adducts initially follows pseudo-first-order kinetics. At the concentration used (5 mmol/L), the samples absorb 100% of the incident light. Hence, the rate constants determined by ^{1}H NMR monitoring give a good comparison of the photoreactivity (Table 2). $\mathbf{1}^{2+}$, $\mathbf{3}^{2+}$, $\mathbf{5}^{2+}$, and $\mathbf{6}^{2+}$ have similar $k_{350-400nm}$ values (3.2×10^{-3} to 5.5×10^{-3} s^{-1}), whereas that of the most reactive complex $\mathbf{4}^{2+}$ is an order of magnitude higher (24.2×10^{-3} s^{-1}). In addition, we used ferrioxalate actinometry[15] to determine the quantum yields of $\mathbf{1}^{2+}$, $\mathbf{3}^{2+}$, and $\mathbf{4}^{2+}$ in the range 350−400 nm and the quantum yield of $\mathbf{4}^{2+}$ at 436 nm. In the range 350−400 nm, the quantum yields of $\mathbf{1}^{2+}$ and $\mathbf{3}^{2+}$ are again similar (0.0054 and 0.0081, respectively), whereas that of $\mathbf{4}^{2+}$ is an order of magnitude higher (0.0360).

DOI: 10.1021/ic502807d
Inorg. Chem. 2015, 54, 4621−4635

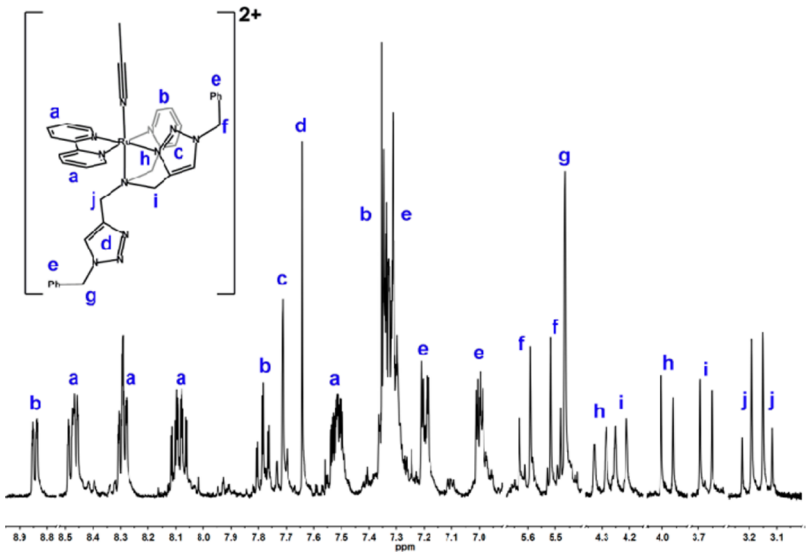

Figure 9. ^{1}H NMR spectrum of $[\mathbf{3}(CD_3CN)]^{2+}$ in CD_3CN. Parts of the spectrum are cut for better visibility of the signals.

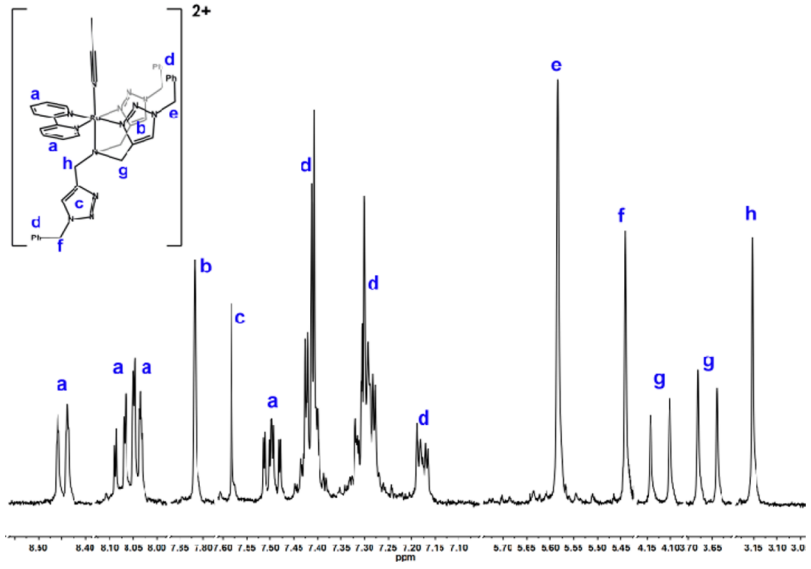

Figure 10. ^{1}H NMR spectrum of $[\mathbf{4}(CD_3CN)]^{2+}$ in CD_3CN. Parts of the spectrum are cut for better visibility of the signals.

At 436 nm, the quantum yield of $\mathbf{4}^{2+}$ is even higher (0.0604), and it is 30 times higher than the value determined for $\mathbf{1}^{2+}$ at 423 nm (0.0021).[7d] We could not determine the quantum yields of $\mathbf{5}^{2+}$ and $\mathbf{6}^{2+}$, because we could not obtain the UV−vis spectra of the pure acetonitrile adducts.

In all cases, the formation of $[\mathbf{X}(CH_3CN)]^{2+}$ under irradiation is only possible when CH_3CN is used as a solvent, because the CH_3CN ligand itself is photolabile. The photoreaction of $\mathbf{4}^{2+}$ in acetone-d_6 with 100 equiv of CH_3CN did not yield any $[\mathbf{4}(CH_3CN)]^{2+}$. When $[\mathbf{4}(CD_3CN)]^{2+}$ was isolated from CD_3CN, redissolved in acetone-d_6, and irradiated for 2 h, the subsequently recorded ^{1}H NMR spectrum showed the signature of $\mathbf{4}^{2+}$. The systems studied by Kojima et al. reacted much more completely to the acetonitrile adduct under thermal activation.[7c,f] Irradiation of these systems never leads to complete conversion to $[\mathbf{X}(CD_3CN)]^{2+}$ (Supporting Information Figure S66). In this regard, the new triazole complex $\mathbf{4}^{2+}$ is the complete opposite of $\mathbf{1}^{2+}$. Irradiation of $\mathbf{4}^{2+}$ leads to the acetonitrile adduct with almost complete conversion within 2 h, and the quantum yield of $\mathbf{4}^{2+}$ is an order of magnitude higher than that of $\mathbf{1}^{2+}$.

Mechanism of the Photoreaction. Kojima et al. suggested that the steric repulsion between the C−H bonds of the equatorial pyridine arm and bpy is the main reason for the reactivity of $\mathbf{1}^{2+}$ (as indicated in Scheme 1). Therefore, the group examined a complex, where one of the pyridine arms of the tripod was substituted with a methyl group. Monitoring the heating experiment of this complex with ^{1}H NMR spectroscopy, they concluded that it is indeed the equatorial TPA arm that dissociates in $\mathbf{1}^{2+}$.[7c]

When either the equatorial pyridine arm (as in $\mathbf{2}^{2+}$) or the pyridines of bpy (as in $\mathbf{7}^{2+}$) are substituted with triazoles, the steric repulsion in the equatorial plane is turned into a weak attraction (vide supra). Whereas this observation does explain the unreactive nature of $\mathbf{2}^{2+}$ and $\mathbf{7}^{2+}$, it does not account for the reactivity of $\mathbf{3}^{2+}$−$\mathbf{6}^{2+}$. Prompted by a report on a Ru^{II} complex with one bpy and two bistriazole ligands,[12] we suspected that

DOI: 10.1021/ic502807d
Inorg. Chem. 2015, 54, 4621−4635

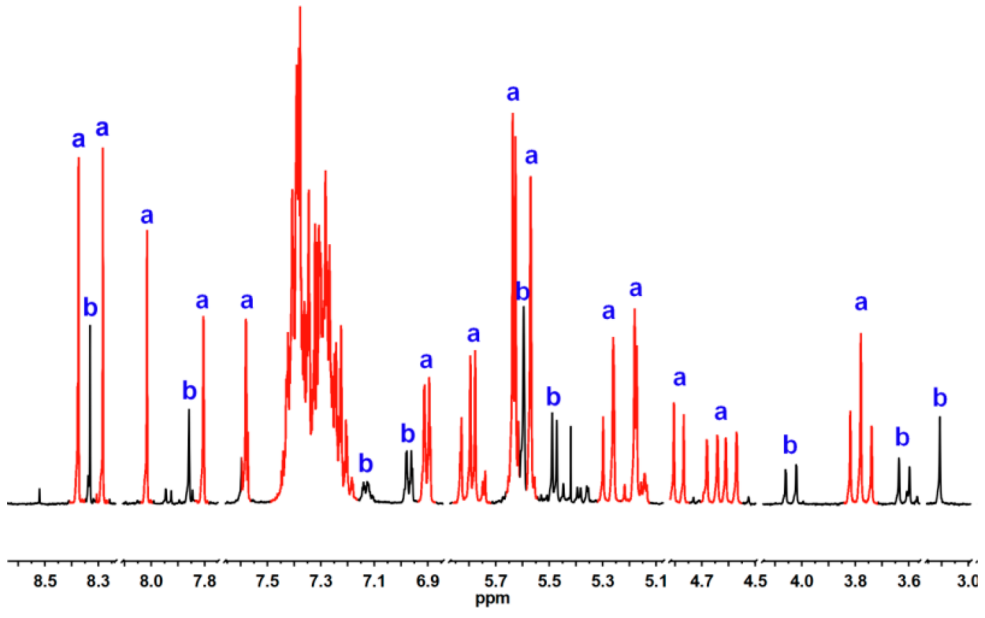

Figure 11. ^{1}H NMR spectrum of $[\mathbf{6a}(CD_3CN)]^{2+}$ (red) and $[\mathbf{6b}(CD_3CN)]^{2+}$ (black) in CD_3CN. Parts of the spectrum are cut for better visibility of the signals.

Scheme 3. Proposed Structures of Acetonitrile Adducts Formed by the Photoreaction of 6^{2+} in CD_3CN

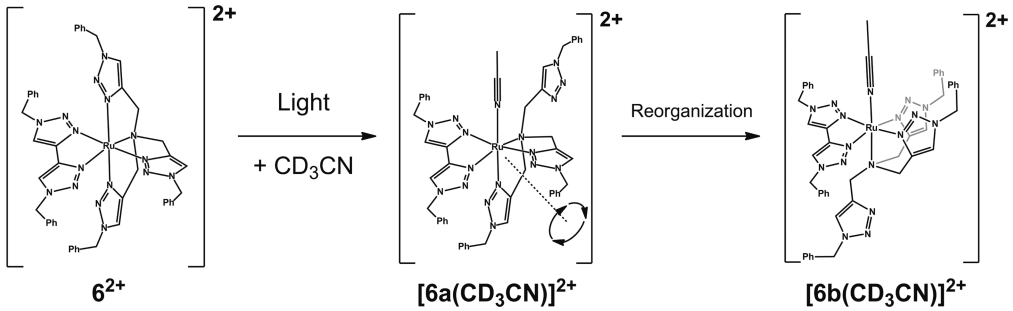

Table 2. Rate Constants and Quantum Yields of the Photoreactions of 1^{2+}–7^{2+}

complex	initial reaction rate constant,[a] k_{init} [10^{-3} s^{-1}]	conversion efficiency[a] [%] (time [min])	quantum yield[b] (350–400 nm), $\phi_{350-400nm}$	quantum yield (monochromatic irradiation), ϕ_λ
$\mathbf{1}^{2+}$	3.2	53 (600)	0.0054	0.0021 (λ = 423 nm)[4]
$\mathbf{2}^{2+}$				
$\mathbf{3}^{2+}$	3.6	87 (960)	0.0081	
$\mathbf{4}^{2+}$	24.2	99 (240)	0.0360	0.0604 (λ = 436 nm)[c]
$\mathbf{5}^{2+}$	4.4	70 (600)		
$\mathbf{6}^{2+}$	5.5	92 (600)		
$\mathbf{7}^{2+}$				

[a]Measured with 5 mmol/L samples (100% absorbance) in NMR tubes with broad-band irradiation (350–400 nm, Supporting Information Figure S62). [b]Determined by using a ferrioxalat actinometer. Samples of $\mathbf{1}^{2+}$ (3.2×10^{-5} mol/L), $\mathbf{3}^{2+}$ (6.7×10^{-5} mol/L), and $\mathbf{4}^{2+}$ (7.4×10^{-5} mol/L) absorbed 66%, 78%, and 48%, respectively, of the light between 350 and 400 nm. [c]Determined by using a ferrioxalat actinometer and monochromated light (spectrofluorimeter source) at 436 nm, where the sample of $\mathbf{4}^{2+}$ (6.3×10^{-5} mol/L) absorbed 46% of the light.

the triazole arms in the axial positions are responsible for the reactivity of $\mathbf{3}^{2+}$–$\mathbf{6}^{2+}$.

Two observations backed up this assumption: there is only one isomer of $[\mathbf{3}(CD_3CN)]^{2+}$, which has a free triazole arm, and the photoreactivity increases from $\mathbf{3}^{2+}$ to $\mathbf{4}^{2+}$. To prove our hypothesis, we synthesized a tripodal ligand (L^5) with two triazole arms bearing a 4-isopropylphenyl residue (i.e., "isopropyl arms") and one triazole arm bearing a simple phenyl residue. With L^5 and bpy, we synthesized complex $\mathbf{8}^{2+}$ (Scheme 4). The ratio of the two isomers $\mathbf{8a}^{2+}$ and $\mathbf{8b}^{2+}$ can be determined from the ^{1}H NMR resonances of the propyl arms in axial and equatorial positions. In the crude product, the $\mathbf{8a}^{2+}$/$\mathbf{8b}^{2+}$ ratio is 70:30, close to the statistically expected value of 2:1.

When $\mathbf{8a}^{2+}$ and $\mathbf{8b}^{2+}$ are irradiated, two different products, $[\mathbf{8a}(CD_3CN)]^{2+}$ and $[\mathbf{8b}(CD_3CN)]^{2+}$, are formed (Scheme 4). The ratio of $[\mathbf{8a}(CH_3CN)]^{2+}$ and $[\mathbf{8b}(CH_3CN)]^{2+}$ can also be determined from the ^{1}H NMR resonances. Unfortunately, a $\mathbf{8a}^{2+}$/$\mathbf{8b}^{2+}$ mixture with a "natural" ratio of 2:1 would yield a 2:1 mixture of $[\mathbf{8a}(CD_3CN)]^{2+}$/$[\mathbf{8b}(CD_3CN)]^{2+}$, both if the

DOI: 10.1021/ic502807d
Inorg. Chem. 2015, 54, 4621–4635

Scheme 4. Isomers of 8^{2+} and $[8(CH_3CN)]^{2+}$

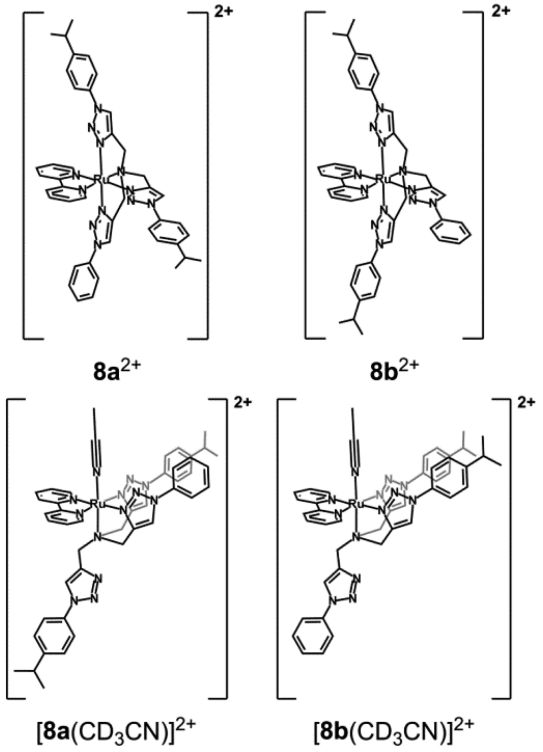

equatorial arm or one of the axial arms dissociates (Supporting Information Scheme S8). Through recrystallization, we obtained $\mathbf{8a}^{2+}/\mathbf{8b}^{2+}$ with a ratio of 28:72. With this mixture, equatorial reactivity should yield $[\mathbf{8a}(CD_3CN)]^{2+}/[\mathbf{8b}(CD_3CN)]^{2+}$ in a ratio of 28:72, whereas axial reactivity should yield $[\mathbf{8a}(CD_3CN)]^{2+}/[\mathbf{8b}(CD_3CN)]^{2+}$ in a ratio of 86:14 (Scheme 5). Experimentally, a 80:20 mixture was obtained. This proves that dissociation (or loosening) of the axial triazole arms is responsible for the reactivity of $\mathbf{3}^{2+}$–$\mathbf{6}^{2+}$, which is in contrast to the dissociation of the equatorial arm in $\mathbf{1}^{2+}$.

Therefore, pyridine arms in axial positions are not photolabile (see $\mathbf{2}^{2+}$ and $\mathbf{7}^{2+}$); the pyridine arm in the equatorial position is only labile when there is steric repulsion (compare $\mathbf{1}^{2+}$ and $\mathbf{7}^{2+}$), and triazole arms in axial positions are photolabile. Hence, by substitution of pyridines with triazoles in the bidentate or tripodal ligand, either the thermo- and photoreactivity reactivity can be turned off (see $\mathbf{2}^{2+}$ and $\mathbf{7}^{2+}$), or the reaction mechanism, time, and completeness can be changed (equatorial vs axial dissociation; slow and incomplete photoreaction in $\mathbf{1}^{2+}$ vs fast and complete photoreaction in $\mathbf{4}^{2+}$).

Redoxreactivity. Measured in CH_3CN, $\mathbf{1}^{2+}$ shows two irreversible oxidation waves at 0.71 and 0.94 V. In addition to the two corresponding rereduction waves, a new small rereduction peak at 0.29 V is observed. It is also observed when the scan direction is reversed right after the oxidation wave at 0.71 V. The intensity of the redox wave at 0.94 V depends on the scan rate, which indicates that it stems from a product of a reaction following the first oxidation process (Figure 12, left). The CV of $[\mathbf{1}(CH_3CN)]^{2+}$ (prepared by

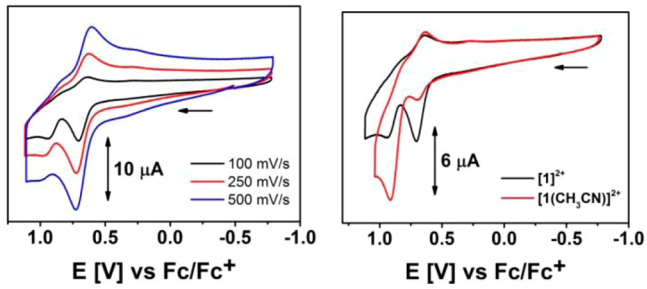

Figure 12. CV of the oxidation of $\mathbf{1}^{2+}$, measured in CH_3CN (0.1 M Bu_4NPF_6) at different scan rates (left). Comparison of the CVs of $\mathbf{1}^{2+}$ and $[\mathbf{1}(CH_3CN)]^{2+}$ measured in CH_3CN at 100 mV/s (right).

Scheme 5. Expected Ratios $[8a(CH_3CN)]^{2+}/[8b(CH_3CN)]^{2+}$ Obtained through Photoactivation by Starting from Mixtures with Different Ratios $8a^{2+}/8b^{2+}$[a]

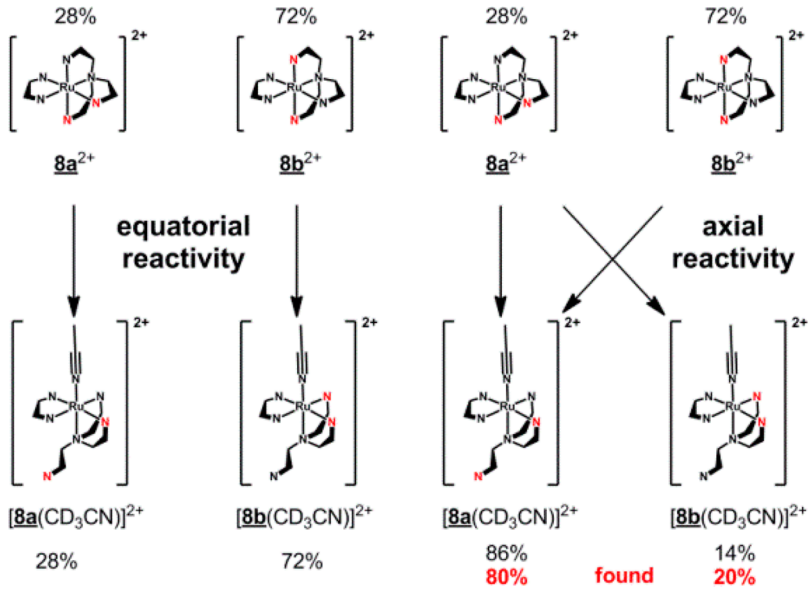

[a]Triazole arms with 4-isopropylphenyl substituents are represented by a red N.

DOI: 10.1021/ic502807d
Inorg. Chem. 2015, 54, 4621−4635

Scheme 6. Proposed Mechanism of the Redox-Triggered Formation of $[\mathbf{1}(CH_3CN)]^{2+}$

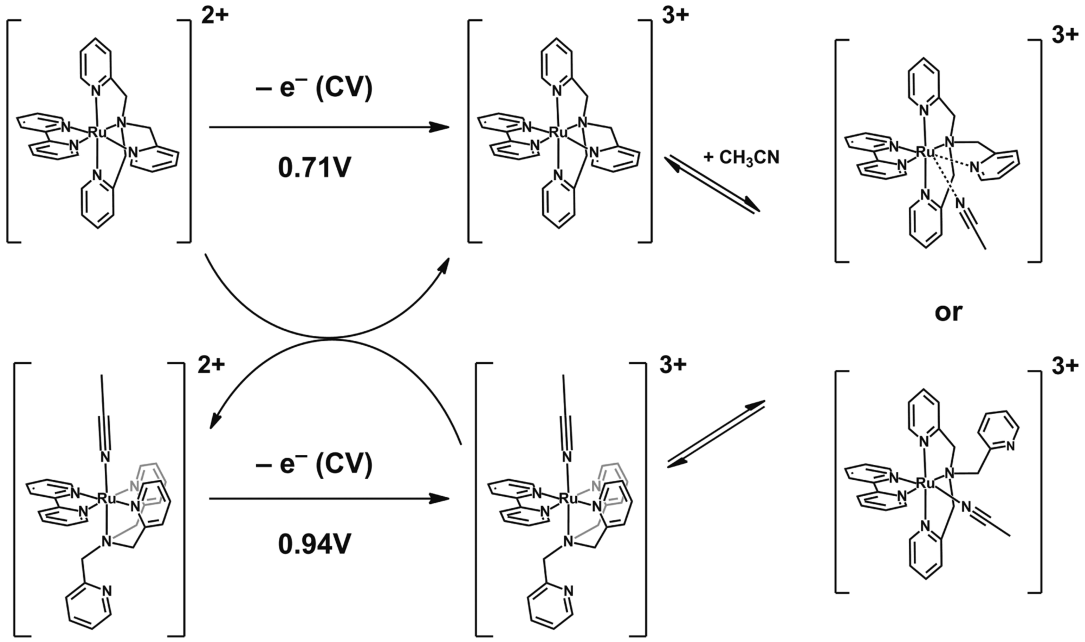

heating) only shows the second oxidation wave (Figure 12, right). Hence, the oxidation of $\mathbf{1}^{2+}$ leads to the formation of $[\mathbf{1}(CH_3CN)]^{2+}$. In the CV of $[\mathbf{1}(CH_3CN)]^{2+}$, the appearance of the new redox couple around 0.33 V is also seen.

In a summary of the above-mentioned observations, the oxidation of $\mathbf{1}^{2+}$ leads to the formation of $[\mathbf{1}(CH_3CN)]^{2+}$, and both the oxidation of $\mathbf{1}^{2+}$ or $[\mathbf{1}(CH_3CN)]^{2+}$ lead to the appearance of a new redox couple around 0.33 V. This can be rationalized by the pathway shown in Scheme 6, which comprises three reactions:

$$\mathbf{1}^{3+} + CH_3CN \rightarrow [\mathbf{1}^*(CH_3CN)]^{3+} \quad (1)$$

$$[\mathbf{1}^*(CH_3CN)]^{3+} \rightarrow [\mathbf{1}(CH_3CN)]^{3+} \quad (2)$$

$$[\mathbf{1}(CH_3CN)]^{3+} + \mathbf{1}^{2+} \rightarrow [\mathbf{1}(CH_3CN)]^{2+} + \mathbf{1}^{3+} \quad (3)$$

In $\mathbf{1}^{3+}$ the decreased electron density at the Ru center leads to less back bonding. Thus, one of the pyridine arms is bound less tightly, and a CH_3CN molecule coordinates to form an intermediate, which is more electron-rich and causes the small redox couple at 0.33 V (eq 1). Because CH_3CN is the solvent, the reaction is of pseudo-first-order. It can be discussed whether $[\mathbf{1}^*(CH_3CN)]^{3+}$ could be a 6-coordinate or 7-coordinate species. As mentioned in the discussion of the photoreactivity, 7-coordinate Ru species are rare and usually observed with smaller ligands.[14] On the other hand, for a 6-coordinate species, where a pyridine arm is simply substituted by a CH_3CN molecule, one would expect the $[\mathbf{1}^*(CH_3CN)]^{2+}/[\mathbf{1}^*(CH_3CN)]^{3+}$ couple to appear at more positive potentials than $\mathbf{1}^{2+}/\mathbf{1}^{3+}$ (according to the electrochemical parameters by Lever).[16] No matter what its exact structure is, $[\mathbf{1}^*(CH_3CN)]^{3+}$ undergoes isomerization to $[\mathbf{1}(CH_3CN)]^{3+}$ (eq 2). Because $[\mathbf{1}(CH_3CN)]^{2+}$ is harder to oxidize than $\mathbf{1}^{2+}$, $[\mathbf{1}(CH_3CN)]^{3+}$ is reduced to $[\mathbf{1}(CH_3CN)]^{2+}$ either at the electrode surface or by excess $\mathbf{1}^{2+}$ in solution (eq 3).

This redox reactivity is mainly observed for $\mathbf{1}^{2+}$, $\mathbf{3}^{2+}$, and $\mathbf{4}^{2+}$. However, small waves corresponding to the acetonitrile adduct and the $[\mathbf{X}^*(CH_3CN)]^{3+}$ intermediate were also observed for $\mathbf{2}^{2+}$. For $\mathbf{5}^{2+}$, small redox waves corresponding to $[\mathbf{X}^*(CH_3CN)]^{3+}$ were observed but no signs of an acetonitrile adduct. For $\mathbf{6}^{2+}$ and $\mathbf{7}^{2+}$, no redox reactivity in acetonitrile could be detected. On the basis of the proposed mechanism, we simulated the CVs of $\mathbf{1}^{2+}$–$\mathbf{4}^{2+}$, $[\mathbf{1}(CH_3CN)]^{2+}$, $[\mathbf{3}(CH_3CN)]^{2+}$, and $[\mathbf{4}(CH_3CN)]^{2+}$ in CH_3CN (Figure 13 and Supporting Information Figures S37–S40).

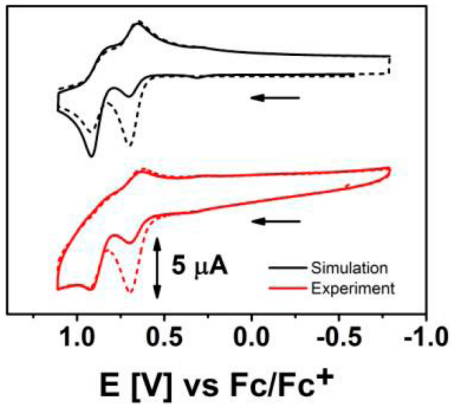

Figure 13. Comparison of the simulated and experimental CVs of $\mathbf{1}^{2+}$ measured in CH_3CN (0.1 M Bu_4NPF_6) at 100 mV/s. Dotted lines mark the first cycle; straight lines mark the second cycle.

To have a reasonable starting point, we estimated the equilibrium constants K_1 and K_2 for the reactions shown in eqs 1 and 2, respectively. According to the work of Nicholson and Shain,[17a] if a reversible chemical reaction precedes a reversible electron transfer, the equilibrium constants can be determined from the ratio of the peak currents of the species in the equilibrium. Hence, we electrolyzed the complexes at high positive potentials and subsequently ran a fast cathodic scan to obtain ratios of $[\mathbf{X}(CH_3CN)]^{3+}$, $\mathbf{X}^{3+}$, and $[\mathbf{X}^*(CH_3CN)]^{3+}$ (Supporting Information Figure S36). Because the waves were very broad at 0.5 V/s, we could only obtain rough estimates for K_1 and K_2. For $\mathbf{1}^{2+}$, K_1 is close to 1, and K_2 is very small. For $\mathbf{3}^{2+}$

DOI: 10.1021/ic502807d
Inorg. Chem. 2015, 54, 4621–4635

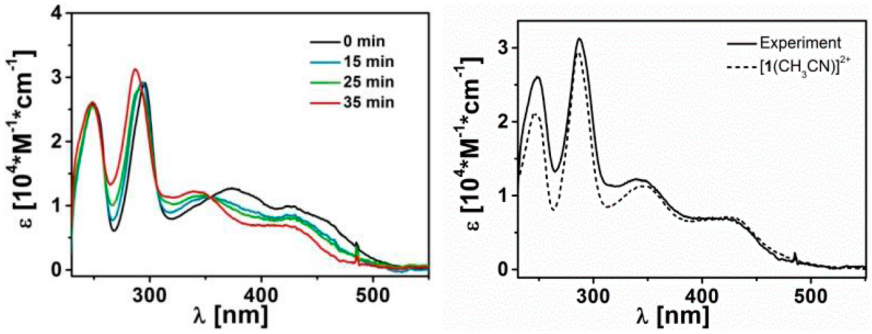

Figure 14. Left: Changes in the UV−vis spectrum of $\mathbf{1}^{2+}$ during electrolysis in DCM/CH_3CN = 99:1 (0.9 V vs Fc/Fc^+, 0.1 M Bu_4PF_6, Pt working electrode, bulk electrolysis cell). Right: Spectrum taken at the end of the bulk electrolysis compared to the spectrum of pure $[\mathbf{1}(CH_3CN)]^{2+}$ in DCM.

and $\mathbf{4}^{3+}$, the K_1 values are around 0.25, and the K_2 values were estimated at 0.4 and 0.8, respectively. The equilibrium constant K_3 of the electron transfer reaction between $[\mathbf{X}(CH_3CN)]^{3+}$ and $\mathbf{X}^{2+}$ depends on the potential gap between the two redox couples and cannot be varied freely in the simulation. For the rate constant k_{f3} of the forward reaction of the ET reaction step, we chose a value of 10^7 L mol^{-1} s^{-1}, which is in the range of values found for Ru complexes in the literature.[17b] Finally, this only leaves k_{f1} and k_{f2} as free parameters, which we varied to fit the first and second cycles of CVs recorded at different scan rates and starting concentrations of $\mathbf{X}^{2+}$ and $[\mathbf{X}(CH_3CN)]^{2+}$. In doing so, we found k_f values between 2.5 and 20 s^{-1} (Supporting Information Table S4), which are in good agreement with values found for similar isomerization reactions of Ru^{II} and Ru^{III} complexes.[17c−e]

When we simulated the redox cycle without the electron transfer step between $\mathbf{X}^{2+}$ and $[\mathbf{X}(CH_3CN)]^{3+}$, that is, we assumed that $[\mathbf{X}(CH_3CN)]^{3+}$ is reduced to $[\mathbf{X}(CH_3CN)]^{2+}$ only at the electrode surface, we could reproduce the first cycles of the CVs but not the second cycles. Hence, the ET step of eq 3 is necessary to fully explain the redox behavior of the complexes. K_1 is biggest for $\mathbf{1}^{2+}$, which can be attributed to the steric repulsion in the equatorial plane (vide supra) that favors a loosening or dissociation the pyridine arm. The unreactive nature of $\mathbf{2}^{2+}$ can be reproduced by assuming a very small K_1 value, which corresponds well to the absence of thermo- and photoreactivity for this complex. For $\mathbf{3}^{2+}$ and $\mathbf{4}^{2+}$, K_1 again increases, which corresponds to the reactivity observed for the axial triazole arms. For the dissociation of an axial arm, the coordinative reorganization (eq 2) consists of a simple rotation (Scheme 3), and it is easier than the dissociation of the equatorial arm. This is reflected by the higher values of K_2 and k_{f2} for $\mathbf{3}^{2+}$ and $\mathbf{4}^{2+}$.

The factor that mostly determines the shape of the CVs and the equilibrium of the overall reaction is the equilibrium constant K_3 of the ET step (eq 3), which in turn is determined by the potential difference between the $\mathbf{X}^{2+}/\mathbf{X}^{3+}$ and $[\mathbf{X}(CH_3CN)]^{2+}/[\mathbf{X}(CH_3CN)]^{3+}$ redox couples. Although K_1 and K_2 are both small for $\mathbf{2}^{2+}$, the large potential gap and K_3 value lead to the appearance of a small $[\mathbf{2}(CH_3CN)]^{2+}/[\mathbf{2}(CH_3CN)]^{3+}$ redox wave. With an increasing number of triazole moieties in the ligands, the acetonitrile species $[\mathbf{X}(CH_3CN)]^{2+}$ become easier to oxidize, and hence the potential gap between the $\mathbf{X}^{2+}$ and $[\mathbf{X}(CH_3CN)]^{2+}$ oxidation decreases. Hence, K_{all} for the overall transformation of $\mathbf{X}^{3+}$ to $[\mathbf{X}(CH_3CN)]^{2+}$ decreases by an order of magnitude from $\mathbf{1}^{2+}$ to $\mathbf{4}^{2+}$. Furthermore, the closing of the potential gap and decrease in K_3 could be the reason why no redox-triggered formation of $[\mathbf{5}(CH_3CN)]^{2+}$ or $[\mathbf{6}(CH_3CN)]^{2+}$ is observed.

According to Scheme 6, it should be possible to convert $\mathbf{X}^{2+}$ to $[\mathbf{X}(CH_3CN)]^{2+}$ by simply generating a catalytic amount of $\mathbf{X}^{3+}$. Therefore, we placed $\mathbf{1}^{2+}$ (4 μmol) in a bulk-electrolysis cell and applied a voltage of 0.9 V (vs Fc/Fc^+) at the working electrode. Upon oxidation, we monitored the UV−vis spectra of the solution and observed the transformation from $\mathbf{1}^{2+}$ to $[\mathbf{1}(CH_3CN)]^{2+}$ (Supporting Information Figure S42). The total charge transferred at the working electrode during the experiment was 14.9 mC, which corresponds to 0.08 μmol of electrons or 2% of the complex molecules. For complexes $\mathbf{3}^{2+}$ and $\mathbf{4}^{2+}$, the redox-triggered mechanism could only be shown in an OTTLE (optically transparent thin-layer electrochemical) cell[18] but not in bulk electrolysis, because the potential gap between $\mathbf{X}^{2+}$ and $[\mathbf{X}(CH_3CN)]^{2+}$, which is the driving force of the cycle, decreases with an increasing number of triazoles.

For $\mathbf{1}^{2+}$, our CV simulations predicted that this conversion should also work when CH_3CN is not the solvent but only present in large excess. Indeed, the redox-triggered mechanism is functional when $\mathbf{1}^{2+}$ was electrolyzed in a DCM/CH_3CN mixture (99:1), although it takes much longer, and a larger amount of oxidized species has to be generated (Figure 14). This is not surprising, because under these conditions (lower CH_3CN concentration) the initial reaction step (eq 1) is no longer pseudo-first-order. However, combined with the observation that irradiation of $[\mathbf{1}(CD_3CN)]^{2+}$ in solvent mixtures with low CH_3CN content leads to the formation of $\mathbf{1}^{2+}$ (vide supra), this redox-triggered conversion could give rise to a switchable system: in the dark, $[\mathbf{1}(CH_3CN)]^{2+}$ could be formed from $\mathbf{1}^{2+}$, catalyzed by small amounts of $\mathbf{1}^{3+}$; upon irradiation, $\mathbf{1}^{2+}$ could form from $[\mathbf{1}(CH_3CN)]^{2+}$ until the light source is turned off. Similar nitrile complexes have already been put to use in the light-triggered release of enzyme inhibitors,[19] and work on the optimization of the necessary switching conditions is currently under way in our laboratory.

CONCLUSIONS

In summary, we have synthesized a series of complexes $[Ru(bident)(tripod)]^{2+}$. The five pyridine rings of $\mathbf{1}^{2+}$ were stepwise substituted with triazole rings ($\mathbf{2}^{2+}$−$\mathbf{7}^{2+}$). In $\mathbf{1}^{2+}$, the dissociation of one tripod arm in CH_3CN can be triggered by heat or light, and $[\mathbf{1}(CH_3CN)]^{2+}$ is formed. Our study confirms that the reactivity of $\mathbf{1}^{2+}$ is due to steric repulsion between the equatorial pyridine arm of the tripodal ligand and bpy. When either the equatorial pyridine arm or bpy is substituted with

DOI: 10.1021/ic502807d
Inorg. Chem. 2015, 54, 4621−4635

triazoles, the repulsion is turned into a weak attraction, and the resulting complexes $\mathbf{2}^{2+}$ and $\mathbf{7}^{2+}$ are completely unreactive.

Further substitution of pyridine rings in complexes $\mathbf{3}^{2+}$–$\mathbf{6}^{2+}$ results in increased photoreactivity compared to that of $\mathbf{1}^{2+}$. In contrast to the TPA-based systems found in the literature, which were optimized toward their thermal reactivity and show incomplete photoreactions, $[\mathbf{4}(CD_3CN)]^{2+}$ was formed by irradiation with 99% conversion efficiency. Hence, by successively substituting pyridine rings with triazoles, we either turned off the reactivity (for $\mathbf{2}^{2+}$) or reversed reaction preferences from thermally activated (complete formation of $[\mathbf{1}(CH_3CN)]^{2+}$) to photoactivated (near complete formation of $[\mathbf{4}(CH_3CN)]^{2+}$). In contrast to the reactivity of the known TPA-based systems, which is based on steric repulsion of the equatorial arm, the new triazole-based systems presented herein react through photodissociation of a triazole arm in an axial position. We were able to prove this mechanism by using the tailor-made ligand L^5 to synthesize and study the photoreactivity of $\mathbf{8}^{2+}$.

In addition to the thermo- and photoreactivity, we discovered a redox-triggered mechanism that provides access to the acetonitrile adduct and is functional in $\mathbf{1}^{2+}$, $\mathbf{3}^{2+}$, and $\mathbf{4}^{2+}$. Catalyzed by a small amount of $\mathbf{X}^{3+}$, it leads to the formation of $[\mathbf{X}(CH_3CN)]^{2+}$ from $\mathbf{X}^{2+}$. We explored the mechanistic details of this conversion by CV simulations, and showed that the mechanism works for $\mathbf{1}^{2+}$ in a bulk-electrolysis cell in pure CH_3CN as well as in DCM/CH_3CN (99:1). Combining this redox-reactivity with the photoreactivity of the complexes could give rise to a switchable system for nitrile release and capture.

EXPERIMENTAL SECTION

General Procedures. All chemicals were commercially available and used as purchased unless otherwise noted. Solvents used for synthesis were dried with appropriate drying agents. All manipulations were carried out under a nitrogen atmosphere unless otherwise noted. The complexes $Ru(DMSO)_4Cl_2$[20a] and $[Ru(bpy)(DMSO)_2Cl_2]$[20b] as well as the ligands TPA (L^1),[20c] L^2, L^3,[8a] TBTA (L^4),[20d] L^7,[20e] and L^8[20f] (Supporting Information Scheme S1) were synthesized according to literature procedures. The synthesis of ligand L^5 is described in the Supporting Information (Scheme S4). *Even though no problems were encountered in the present work, the azides used for the ligand synthesis are potentially explosive compounds and should be handled with care.* ^{1}H NMR data were recorded with a Jeol Lambda 400 (400 MHz) and a Bruker AVANCE700 (700 MHz) by using the chemical shift of the solvent as an internal standard. X-band EPR spectra were recorded at room temperature with an EMX Bruker system connected to an ER 4131 VT variable-temperature accessory. The EPR samples were electrolyzed with a platinum-wire working electrode and a platinum-wire counterelectrode. Elemental analyses (CHN) were measured with an Elementar Vario EL III; the high fluorine content of the samples (two PF_6^-) negatively affected the accuracy of the hydrogen values. Mass spectra were recorded with an Agilent 6210 ESI-TOF spectrometer (Agilent Technologies, Santa Clara, CA).

Electrochemistry. Cyclic voltammograms were recorded with a PAR VersaStat 4 potentiostat (Ametek) by working in anhydrous dichloromethane ($H_2O \leq 0.005\%$, puriss, SigmaAldrich) or acetonitrile ($H_2O \leq 0.01\%$, puriss, SigmaAldrich) distilled from calcium hydride or calcium chloride, respectively. A three-electrode setup was used with a glassy-carbon working electrode, a coiled platinum wire as the counter electrode, and a coiled silver wire as the pseudoreference. Ferrocene or decamethylferrocene were used as an internal standard, and 0.1 m NBu_4PF_6 (Fluka, ≥99.0%, electrochemical grade) was used as an electrolyte. Simulations of the CV data were carried out with the software DigiElch Professional (Version 7.FD), and details of the simulation are given in the Supporting Information. Bulk electrolyses were carried out in a cell with three compartments separated by frits for the Pt-sheet working electrode, the coiled-Pt-wire counter electrode, and the coiled-silver-wire pseudoreference.

UV–Vis Spectroscopy and Spectroelectrochemistry. UV–vis spectra were recorded with an Avantes spectrometer consisting of a light source (AvaLight-DH-S-Bal), a UV–vis detector (AvaSpec-ULS2048) and a NIR detector (AvaSpec-NIR256-TEC). UV–vis spectroelectrochemistry measurements were carried out in an optically transparent thin-layer electrochemical (OTTLE) cell[18] with a platinum-mesh working electrode, an platinum-mesh counter electrode, and a silver-foil pseudo reference.

Reactivity Experiments and Actinometry. The reactivity experiments of the complexes were carried out in deuterated acetonitrile in NMR tubes sealed with parafilm with complex concentrations of 5 mmol/L. The NMR tubes were either heated at 80 °C in an oil bath or irradiated with a 4 W UV lamp (UVGL-25, UVP, Upland, CA). The emission profile of the lamp is shown in Supporting Information Figure S62. It emits light in the range 350–400 nm with a maximum at 369 nm and a bandwidth-at-half-maximum of 16 nm, which is comparable to light sources used for analogous Ru^{II} complexes.[7f] An aqueous ferrioxalate solution (0.006 mol/L)[15a,b] and solutions of $\mathbf{1}^{2+}$ (3.2×10^{-5} mol/L), $\mathbf{3}^{2+}$ (6.7×10^{-5} mol/L), and $\mathbf{4}^{2+}$ (7.4×10^{-5} mol/L) in acetonitrile were placed in standard quartz cuvettes (1 cm) directly in front of the lamp. The use of a "broadband" light source is permissible for actinometry if the fraction of light that is absorbed by the ferrioxalate standard and the complex solutions in the respective spectral range is taken into account;[15a] indeed, the "monochromated" light used to determine the quantum yields of similar Ru^{II} complexes often actually covers a range of 20 nm or more.[7f,g] A 0.006 mmol/L ferrioxalate solution absorbs 100% of the incident light between 350 and 400 nm,[15b] whereas the solutions of complexes $\mathbf{1}^{2+}$, $\mathbf{3}^{2+}$, and $\mathbf{4}^{2+}$ absorbed 66%, 78%, and 48%, respectively. At the emission maximum of the "broadband" light source (369 nm), the quantum yield of ferrioxalate is 1.21 and varies only slightly (1.23 at 334 nm and 1.13 at 392 nm).[15a] The number of photons absorbed by the ferrioxalate solution was determined at 2.6×10^{-8} mol/s. The emission profile of the lamp and the absorbance of the sample solutions were used to determine the fractions of light absorbed by the solutions of $\mathbf{1}^{2+}$, $\mathbf{3}^{2+}$, and $\mathbf{4}^{2+}$ (66%, 78%, and 48%, respectively). The absorbances of the complexes at 470 nm were used to monitore the progress of the reaction. The error resulting from the different refractive indices of water (for ferrioxalate) and acetonitrile (samples) is negligible.[15c] For $\mathbf{4}^{2+}$, the quantum yield was determined at 436 nm by using the light source of a Cary Eclipse fluorescence spectrophotometer (Agilent). The number of photons absorbed by the ferrioxalate solution (absorbs ca. 50% of the light at 436 nm) was determined at 3.3046×10^{-10} mol/s. The solution of $\mathbf{4}^{2+}$ in acetonitrile (6.3×10^{-5} mol/L) absorbed 46% of the light.

X-ray Crystallography. Single crystals suitable for X-ray diffraction analysis were obtained by slow vapor diffusion of Et_2O into concentrated solutions of $\mathbf{2}^{2+}$, $\mathbf{3}^{2+}$, $\mathbf{4}^{2+}$, or $\mathbf{7}^{2+}$ in methanol. Single crystal X-ray diffraction data were collected with a Bruker Smart AXS diffractometer. Data were collected at 100(2) K by using graphite-monochromated Mo Kα radiation (λ = 0.710 73 Å). The strategy for the data collection was evaluated by using the CrysAlisPro CCD software. The data were collected by the standard ψ–ω scan techniques and were scaled and reduced by using CrysAlisPro RED software. The structures were solved by direct methods using SHELXS-97 and refined by full-matrix least-squares with SHELXL-97, refining on F^2.[21]

The positions of all the atoms were obtained by direct methods. All non-hydrogen atoms were refined anisotropically. The remaining hydrogen atoms were placed in geometrically constrained positions and refined with isotropic temperature factors, generally 1.2 times the U_{eq} values of their parent atoms. Supporting Information Table S2 contains the parameters for the data collection and refinement.

CCDC-918972 (for $\mathbf{2}^{2+}$), -918973 (for $\mathbf{3}^{2+}$), -919874 (for $\mathbf{4}^{2+}$), and -1015560 (for $\mathbf{7}^{2+}$) contain the crystallographic information for this paper. All these data can be obtained free of charge from the Cambridge Crystallographic Data Centre via www.ccdc.cam.ac.uk/data_request/cif.

DOI: 10.1021/ic502807d
Inorg. Chem. 2015, 54, 4621–4635

DFT Calculations. The program package ORCA 3.0.0 was used for all DFT calculations.[22a] The geometry optimizations were performed by using DFT methods with the BP86 functional[22b,c] and by including relativistic effects in zero-order regular approximation (ZORA).[22d] Convergence criteria for the geometry optimizations were set to default values (OPT), and "tight" convergence criteria were used for SCF calculations (TIGHTSCF). Triple- ζ valence quality basis sets (def2-TZVP) were used for all atoms.[22e] The resolution of the identity approximation (RI-J) was employed[22f−j] with matching auxiliary basis sets.[22k,l]

Synthesis. *[Ru(L^1)(bpy)](PF$_6$)$_2$ {1(PF$_6$)$_2$}.* [Ru(bpy)(DMSO)$_2$Cl$_2$] (81 mg, 0.17 mmol), TPA (L^1) (50 mg, 0.17 mmol), and KPF_6 (80 mg, 0.43 mmol) were heated overnight at 150 °C in ethylene glycol (10 mL), which was purged with nitrogen prior to the reaction. After the mixture had cooled down to room temperature, water (20 mL) and excess KPF_6 (312 mg, 1.7 mmol) were added to induce precipitation of the product. The orange precipitate was filtered off and redissolved in acetone/DCM (1:1, 15 mL). The organic phase was washed three times with water (5 mL) and dried over Na_2SO_4. The solvents were removed under reduced pressure, and the resulting crude solid was purified by column chromatography on aluminum oxide. After starting with pure DCM, the eluent was slowly changed to DCM/methanol (98:2) to extract the product. Evaporation of the solvent under reduced pressure yielded the pure product (116 mg, 82% yield). $C_{28}H_{26}N_6P_2F_{12}Ru$: Calcd C 40.15, H 3.13, N 10.03; Found C 40.28, H 4.09, N 10.07. UV−vis (DCM): λ [nm] (ε [M^{-1} cm^{-1}]) = 249 (28 210), 295 (31 010), 370 (13 880), 425 (11 930), 452 (10 090) sh. For ^{1}H NMR assignment see the Supporting Information.

[Ru(L^2)(bpy)](PF$_6$)$_2$ {2(PF$_6$)$_2$}. The complex was prepared analogously to **1**(PF$_6$)$_2$. [Ru(bpy)(DMSO)$_2$Cl$_2$] (97 mg, 0.20 mmol), L^2 (74 mg, 0.20 mmol), and KPF_6 (92 mg, 0.50 mmol) yielded pure **2**(PF$_6$)$_2$ after column chromatography (143 mg, 78% yield). $C_{32}H_{30}N_8P_2F_{12}Ru\cdot 1.5H_2O$: Calcd C 40.69, H 3.48, N 11.86; Found C 40.70, H 3.23, N 11.81. UV−vis (DCM): λ [nm] (ε [M^{-1} cm^{-1}]) = 249 (23 760), 295 (33 400), 337 (12 050) sh, 384 (14 370), 457 (8760). For ^{1}H NMR assignment see the Supporting Information.

[Ru(L^3)(bpy)](PF$_6$)$_2$ {3(PF$_6$)$_2$}. The complex was prepared analogously to **1**(PF$_6$)$_2$. However, after addition of water and excess KPF_6, precipitation was not complete, and the precipitate was too fine to be filtered off completely. The ethylene glycol/water phase was therefore extracted with acetone/DCM (1:1, 15 mL) three times. The combined organic phases were washed with water (15 mL) once and dried over Na_2SO_4. After evaporation of the solvents under reduced pressure, the resulting orange crude product was purified by column chromatography analogously to **1**(PF$_6$)$_2$. [Ru(bpy)(DMSO)$_2$Cl$_2$] (97 mg, 0.15 mmol), L^3 (68 mg, 0.15 mmol), and KPF_6 (80 mg, 0.43 mmol) yielded pure **3**(PF$_6$)$_2$ (127 mg, 85% yield). $C_{36}H_{34}N_{10}P_2F_{12}Ru\cdot 1.1H_2O$: Calcd C 42.49, H 3.59, N 13.77; Found C 42.54, H 3.48, N 13.71. UV−vis (DCM): λ [nm] (ε [M^{-1} cm^{-1}]) = 250 (16 140), 293 (33 030), 334 (11 690), 367 (10 530) sh, 450 (6810). For ^{1}H NMR assignment see the Supporting Information.

[Ru(L^4)(bpy)](PF$_6$)$_2$ {4(PF$_6$)$_2$}. The complex was prepared analogously to **3**(PF$_6$)$_2$. [Ru(bpy)(DMSO)$_2$Cl$_2$] (97 mg, 0.20 mmol), L^4 (106 mg, 0.20 mmol), and KPF_6 (92 mg, 0.50 mmol) yielded **4**(PF$_6$)$_2$. Because evaporation of the solvent from the eluted product fraction only yielded the product as an oily solid, **4**(PF$_6$)$_2$ was precipitated by adding a concentrated solution of the complex in acetone to an excess volume of Et_2O, which afforded an orange powder (166 mg, 77% yield). $C_{40}H_{38}N_{12}P_2F_{12}Ru\cdot Et_2O$: Calcd C 45.88, H 4.20, N 14.59; Found C 46.34, H 4.65, N 15.27. UV−vis (DCM): λ [nm] (ε [M^{-1} cm^{-1}]) = 245 (10 830), 255 (10 040) sh, 292 (29 980), 326 (11 800) sh, 446 (4920). For ^{1}H NMR assignment see the Supporting Information.

[Ru(L^4)(L^7)](PF$_6$)$_2$ {5(PF$_6$)$_2$}. [Ru(DMSO)$_4$Cl$_2$] (0.5 mmol, 242 mg) and L^7 (0.5 mmol, 118 mg) were heated at reflux for 2 h in an ethanol/DMSO mixture (9:1, 10 mL). The mixture was allowed to cool down, and crude [Ru(L^7)(DMSO)$_2$Cl$_2$] was filtered off as a yellow precipitate and washed with cold ethanol. The crude product was used without further purification (152 mg, 54% yield). ^{1}H NMR (400 MHz, DMSO-d_6): δ = 9.51 (d, J = 5.9 Hz, 1H, *py*−triazole), 8.47 (s, 1H, py−*triazole*), 7.39 (d, J = 7.3 Hz 1H, *py*−triazole), 7.27 (t, J = 7.3 Hz, 1H, *py*−triazole), 6.76 (t, J = 7.3 Hz, 1H, *py*−triazole), 6.67−6.56 (m, 5H, *Ph*−CH_2−triazole), 5.08 (s, 2H, Ph−CH_2−triazole), 2.59 (s, 12H, Ru−*DMSO*) ppm. MS (+ESI): m/z = 588.9678 [M + Na]$^+$.

The target complex was prepared analogously to **3**(PF$_6$)$_2$. [Ru(L^7)(DMSO)$_2$Cl$_2$] (56 mg, 0.10 mmol), L^4 (53 mg, 0.10 mmol), and KPF_6 (46 mg, 0.25 mmol) afforded pure **5**(PF$_6$)$_2$ (85 mg, 73% yield) as a yellow solid after column chromatography. $C_{44}H_{42}N_{14}P_2F_{12}Ru\cdot 0.7H_2O$: Calcd C 45.15, H 3.74, N 16.75; Found C 45.30, H 3.89, N 16.60. UV−vis (DCM): λ [nm] (ε [M^{-1} cm^{-1}]) = 236 (13 570), 274 (25 460), 320 (15 410), 386 (7630). For ^{1}H NMR assignment see the Supporting Information.

[Ru(L^4)(L^8)](PF$_6$)$_2$ {6(PF$_6$)$_2$}. [Ru(DMSO)$_4$Cl$_2$] (0.5 mmol, 242 mg) and L^8 (0.5 mmol, 158 mg) were heated at reflux for 2 h in an ethanol/DMSO mixture (9:1, 10 mL). The mixture was allowed to cool down, and crude [Ru(L^8)(DMSO)$_2$Cl$_2$] was filtered off as a light yellow precipitate and washed with cold ethanol. The crude product was used without further purification (202 mg, 63% yield). ^{1}H NMR (400 MHz, DMSO-d_6): δ = 7.97 (s, 2H, Ph−CH_2−*triazole*), 6.64−6.53 (m, 10H, *Ph*−CH_2−triazole), 5.02 (s, 4H, Ph−CH_2−triazole) ppm. MS (+ESI): m/z = 667.0032 [M + Na]$^+$.

The target complex was prepared analogously to **3**(PF$_6$)$_2$. [Ru(L^8)(DMSO)$_2$Cl$_2$] (64 mg, 0.10 mmol), L^4 (53 mg, 0.10 mmol), and KPF_6 (46 mg, 0.25 mmol) afforded **6**(PF$_6$)$_2$. Because evaporation of the solvent from the eluted product fraction only yielded the product as an oily solid, **6**(PF$_6$)$_2$ was precipitated by adding a concentrated solution of the complex in acetone to an excess volume of Et_2O, which afforded an almost colorless powder (83 mg, 67% yield). $C_{48}H_{46}N_{16}P_2F_{12}Ru\cdot Et_2O$: Calcd C 47.60, H 4.30, N 17.08; Found C 48.10, H 4.35, N 17.58. UV−vis (DCM): λ [nm] (ε [M^{-1} cm^{-1}]) = 233 (30 630), 325 (25 180). For ^{1}H NMR assignment see the Supporting Information.

[Ru(L^1)(L^8)](PF$_6$)$_2$ {7(PF$_6$)$_2$}. The target complex was prepared analogously to **6**(PF$_6$)$_2$. [Ru(L^8)(DMSO)$_2$Cl$_2$] (64 mg, 0.10 mmol), L^1 (29 mg, 0.10 mmol), and KPF_6 (46 mg, 0.25 mmol) afforded **7**(PF$_6$)$_2$. Because evaporation of the solvent from the eluted product fraction only yielded the product as an oily solid, **7**(PF$_6$)$_2$ was precipitated by adding a concentrated solution of the complex in acetone to an excess volume of Et_2O, which afforded a yellow powder (90 mg, 90% yield). $C_{36}H_{34}N_{10}P_2F_{12}Ru\cdot Et_2O\cdot H_2O$: Calcd C 44.08, H 4.25, N 12.85; Found C 43.80, H 4.47, N 12.68. UV−vis (DCM): λ [nm] (ε [M^{-1} cm^{-1}]) = 240 (18 480), 286 (4670) sh, 378 (11400), 417 (5630) sh. For ^{1}H NMR assignment see the Supporting Information.

[Ru(L^5)(bpy)](PF$_6$)$_2$ {8(PF$_6$)$_2$}. The complex was prepared analogously to **3**(PF$_6$)$_2$. [Ru(bpy)(DMSO)$_2$Cl$_2$] (97 mg, 0.20 mmol), L^5 (114 mg, 0.20 mmol), and KPF_6 (92 mg, 0.50 mmol) yielded pure **8**(PF$_6$)$_2$ (186 mg, 83% yield). The ratio of the two isomers **8a**$^{2+}$/**8b**$^{2+}$ after the first column chromatography was 70:30, which is close to the expected statistical distribution of 2:1 or 67:33. Attempts to separate the isomers by slow careful column chromatography, that is, collecting the eluted product in several test tubes and recording ^{1}H NMR spectra of the fraction in each test tube, only afforded a **8a**$^{2+}$/**8b**$^{2+}$ mixture of 60:40. However, when the compound was recrystallized from a concentrated solution in acetone by adding Et_2O and keeping the solution in the freezer (−20 °C), the first fraction of crystalline material showed a **8a**$^{2+}$/**8b**$^{2+}$ ratio of 28:72.

$C_{43}H_{44}N_{12}P_2F_{12}Ru\cdot 0.2Et_2O$: Calcd C 46.36, H 4.09, N 14.81; Found C 46.55, H 4.19, 14.98. UV−vis (DCM): λ [nm] (ε [M^{-1} cm^{-1}]) = 245 (36 164), 291 (35 556), 347 (23 196), 441 (7010). For ^{1}H NMR assignment see the Supporting Information.

[Ru(L^1)(bpy)(CD$_3$CN)](PF$_6$)$_2$ {[1(CD$_3$CN)](PF$_6$)$_2$}. A solution of **1**(PF$_6$)$_2$ in CD_3CN (0.7 mL, 5 mmol/L) was put in an NMR tube and heated in an oil bath at 80 °C for 2 days. After the solution had cooled down a ^{1}H NMR spectrum was recorded, which was identical to that of pure [**1**(CD$_3$CN)]$^{2+}$ known from the literature.[7d] UV−vis (CH_3CN): λ [nm] (ε [M^{-1} cm^{-1}]) = 247 (25 259), 286 (33 304), 347 (11 938), 427 (6951). For ^{1}H NMR assignment see the Supporting Information.

DOI: 10.1021/ic502807d
Inorg. Chem. 2015, 54, 4621−4635

[Ru(L³)(bpy)(CD₃CN)](PF₆)₂ {[3(CD₃CN)](PF₆)₂}. A solution of **3**$(PF_6)_2$ in CD_3CN (0.7 mL, 5 mmol/L) was put in an NMR tube and irradiated at 350−400 nm. The reaction was monitored by ^1H NMR, and after 16 h a maximum amount of 87% of the original complex had reacted to a new species, the ^1H NMR resonances of which could be attributed to $[\mathbf{3}(CD_3CN)]^{2+}$ (see discussion of the photoreactivity). A sample of the NMR solution was taken and diluted with nondeuterated CH_3CN (20× the volume). A few drops of this solution were further diluted with DCM, and ESI mass spectra were measured. MS (+ESI): m/z = 897.2095 [Ru + L^3 + bpy + CD_3CN + PF_6]$^+$. UV−vis (CH_3CN): λ [nm] (ε [M^{-1} cm^{-1}]) = 246 (15 859), 252 (15 588), 286 (32 932), 326 (10 633) sh, 424 (5960). For ^1H NMR assignment see the Supporting Information.

[Ru(L⁴)(bpy)(CD₃CN)](PF₆)₂ {[4(CD₃CN)](PF₆)₂}. A solution of **4**$(PF_6)_2$ in CD_3CN (0.7 mL, 5 mmol/L) was put in an NMR tube and irradiated at 350−400 nm. The reaction was monitored by ^1H NMR, and after 4 h all of the original complex had reacted to a new species, the ^1H NMR resonances of which could be attributed to $[\mathbf{4}(CD_3CN)]^{2+}$ (see discussion of the photoreactivity). The complex was precipitated from the solution by adding Et_2O, and mass spectra were measured from a solution of $[\mathbf{4}(CD_3CN)]^{2+}$ in DCM. MS (+ESI): m/z = 977.2484 [Ru + L^4 + bpy + CD_3CN + PF_6]$^+$. UV−vis (CH_3CN): λ [nm] (ε [M^{-1} cm^{-1}]) = 243 (10 702), 252 (9868), 286 (30 088), 316 (11 513), 427 (4653). For ^1H NMR assignment see the Supporting Information.

[Ru(L⁴)(L⁷)(CD₃CN)](PF₆)₂ {[5(CD₃CN)](PF₆)₂}. A solution of **5**$(PF_6)_2$ in CD_3CN (0.7 mL, 5 mmol/L) was put in an NMR tube and irradiated at 350−400 nm. The reaction was monitored by ^1H NMR, and after 13 h a maximum amount of 68% of the original complex had reacted to a new species, the ^1H NMR resonances of which could be attributed to $[\mathbf{5}(CD_3CN)]^{2+}$. A sample of the NMR solution was taken and diluted with nondeuterated CH_3CN (20× the volume). A few drops of this solution were further diluted with DCM, and ESI mass spectra were measured. MS (+ESI): m/z = 1057.2835 [Ru + L^4 + L^7 + CD_3CN + PF_6]$^+$. For ^1H NMR assignment see the Supporting Information.

[Ru(L⁴)(L⁸)(CD₃CN)](PF₆)₂ {[6(CD₃CN)](PF₆)₂}. A solution of **6**$(PF_6)_2$ in CD_3CN (0.7 mL, 5 mmol/L) was put in an NMR tube and irradiated at 350−400 nm. The reaction was monitored by ^1H NMR, and after 10 h a maximum amount of 92% of the original complex had reacted to two new species, the ^1H NMR resonances of which could be attributed to $[\mathbf{6a}(CD_3CN)]^{2+}$ and $[\mathbf{6b}(CD_3CN)]^{2+}$ (see discussion of the photoreactivity). A sample of the NMR solution was taken and diluted with nondeuterated CH_3CN (20× the volume). A few drops of this solution were further diluted with DCM, and ESI mass spectra were measured. MS (+ESI): m/z = 1137.3210 [Ru + L^4 + L^8 + CD_3CN + PF_6]$^+$. For ^1H NMR assignment see the Supporting Information.

[Ru(L⁵)(bpy)(CD₃CN)](PF₆)₂ {[8(CD₃CN)](PF₆)₂}. A solution of **8a**$(PF_6)_2$/**8b**$(PF_6)_2$ (28:72) in CD_3CN (0.7 mL, 5 mmol/L) was put in an NMR tube and irradiated at 350−400 nm. The reaction was monitored by ^1H NMR, and after 2 h all of the original complex molecules had reacted to two new species, the ^1H NMR resonances of which could be attributed to $[\mathbf{8a}(CD_3CN)]^{2+}$/$[\mathbf{8b}(CD_3CN)]^{2+}$ (80:20) (see discussion of the photoreaction mechanism). For ^1H NMR assignment see the Supporting Information.

■ ASSOCIATED CONTENT

Supporting Information

X-ray crystallographic data of **2**$(PF_6)_2$·0.25H2O, **3**$(PF_6)_2$·MeOH, **4**$(PF_6)_2$·0.25MeOH, and **7**$(PF_6)_2$·MeOH in CIF format. X-ray diffraction, ^1H NMR, EPR, UV−vis, CV, and spectroelectrochemistry data and details of the reactivity studies and CV simulations. The Supporting Information is available free of charge on the ACS Publications website at DOI: 10.1021/ic502807d.

■ AUTHOR INFORMATION

Corresponding Author

*E-mail: biprajit.sarkar@fu-berlin.de.

Notes

The authors declare no competing financial interest.

■ ACKNOWLEDGMENTS

Fonds der Chemischen Industrie (FCI) and the Freie Universität Berlin are kindly acknowledged for the financial support of this work. We are grateful to Prof. Dr. W. Kaim (Universität Stuttgart) for access to the EPR facilities there. The computer facilities of the Freie Universitat Berlin (ZEDAT) are acknowledged for computation time.

■ REFERENCES

(1) (a) Nazeeruddin, M. K.; Angelis, F.; De Fantacci, S.; Selloni, A.; Viscardi, G.; Liska, P.; Ito, S.; Takeru, B.; Grätzel, M. *J. Am. Chem. Soc.* **2005**, *127*, 16835. (b) Nazeeruddin, M. K.; Péchy, P.; Renouard, T.; Zakeeruddin, S. M.; Humphry-Baker, R.; Comte, P.; Liska, P.; Cevey, L.; Costa, E.; Shklover, V.; Spiccia, L.; Deacon, G. B.; Bignozzi, C. A.; Grätzel, M. *J. Am. Chem. Soc.* **2001**, *123*, 1613.

(2) Among others: (a) Zeitler, K. *Angew. Chem., Int. Ed.* **2009**, *48*, 9785. (b) Zen, J.-M.; Liou, S.-L.; Kumar, A. S.; Hsia, M.-S. *Angew. Chem., Int. Ed.* **2003**, *42*, 577. (c) Berardi, S.; Ganga, G.; La Natali, M.; Bazzan, I.; Puntoriero, F.; Sartorel, A.; Scandola, F.; Campagna, S.; Bonchio, M. *J. Am. Chem. Soc.* **2012**, *134*, 11104. (d) Na, Y.; Wang, M.; Pan, J.; Zhang, P.; Akermark, B.; Sun, L. *Inorg. Chem.* **2008**, *47*, 2805. (e) Sakai, K.; Ozawa, H. *Coord. Chem. Rev.* **2007**, *251*, 2753. (f) Sano, Y.; Onoda, A.; Hayashi, T. *Chem. Commun.* **2011**, *47*, 8229. (g) Shan, B.; Baine, T.; Ma, X. A. N.; Zhao, X.; Schmehl, R. H. *Inorg. Chem.* **2013**, *52*, 4853. (h) Shimakoshi, H.; Tokunaga, M.; Baba, T.; Hisaeda, Y. *Chem. Commun.* **2004**, 1806.

(3) Among others: (a) Weisser, F.; Huebner, R.; Schweinfurth, D.; Sarkar, B. *Chem.—Eur. J.* **2011**, *17*, 5727. (b) Ward, M. D. *J. Solid State Electrochem.* **2005**, *9*, 778. (c) Ghumaan, S.; Sarkar, B.; Maji, S.; Puranik, V. G.; Fiedler, J.; Urbanos, F. A.; Jimenez-Aparicio, R.; Kaim, W.; Lahiri, G. K. *Chem.—Eur. J.* **2008**, *14*, 10816. (d) Das, H. S.; Schweinfurth, D.; Fiedler, J.; Khusniyarov, M. M.; Mobin, S. M.; Sarkar, B. *Chem.—Eur. J.* **2014**, *20*, 4334. (e) Das, H. S.; Das, A. K.; Pattacini, R.; Hübner, R.; Sarkar, B.; Braunstein, P. *Chem. Commun.* **2009**, 4387. (f) Das, H. S.; Weisser, F.; Schweinfurth, D.; Su, C.-Y.; Bogani, L.; Fiedler, J.; Sarkar, B. *Chem.—Eur. J.* **2010**, *16*, 2977.

(4) Ishizuka, T.; Tobita, K.; Yano, Y.; Shiota, Y.; Yoshizawa, K.; Fukuzumi, S.; Kojima, T. *J. Am. Chem. Soc.* **2011**, *133*, 18570.

(5) (a) Yamaguchi, M.; Kousaka, H.; Izawa, S.; Ichii, Y.; Kumano, T.; Masui, D.; Yamagishi, T. *Inorg. Chem.* **2006**, *45*, 8342. (b) Ohzu, S.; Ishizuka, T.; Hirai, Y.; Fukuzumi, S.; Kojima, T. *Chem.—Eur. J.* **2013**, *19*, 1563.

(6) Among others: (a) Radaram, B.; Ivie, J. A.; Singh, W. M.; Grudzien, R. M.; Reibenspies, J. H.; Webster, C. E.; Zhao, X. *Inorg. Chem.* **2011**, *50*, 10564. (b) Ledney, M.; Dutta, P. K. *J. Am. Chem. Soc.* **1995**, *117*, 7687. (c) Duan, L. L.; Xu, Y.-H.; Zhang, P.; Wang, M.; Sun, L.-C. *Inorg. Chem.* **2010**, *49*, 209. (d) Pushkar, Y.; Moonshiram, D.; Purohit, V.; Yan, L.; Alperovich, I. *J. Am. Chem. Soc.* **2014**, *136*, 11938. (e) Gersten, S. W.; Samuels, G. J.; Meyer, T. J. *J. Am. Chem. Soc.* **1982**, *104*, 4029.

(7) (a) Seeberg-Kraft, S.; Bischof, C.; Loos, A.; Braun, S.; Jafarova, J.; Schatzschneider, U. *J. Inorg. Biochem.* **2009**, *103*, 1126. (b) Hilt, G.; Jarbawi, T.; Heineman, W. R.; Steckhan, E. *Chem.—Eur. J.* **1997**, *3*, 79. (c) Kojima, T.; Morimoto, T.; Sakamoto, T.; Miyazaki, S.; Fukuzumi, S. *Chem.—Eur. J.* **2008**, *14*, 8904. (d) Kojima, T.; Nakayama, K.; Sakaguchi, M.; Ogura, T.; Ohkubo, K.; Fukuzumi, S. *J. Am. Chem. Soc.* **2011**, *133*, 17901. (e) Kojima, T.; Nakayama, K.; Ikemura, K.-I.; Ogura, T.; Fukuzumi, S. *J. Am. Chem. Soc.* **2011**, *133*, 11692. (f) Sawaki, T.; Ishizuka, T.; Kawano, M.; Shiota, Y.; Yoshizawa, K.; Kojima, T. *Chem.—Eur. J.* **2013**, *19*, 8978. (g) Miyazaki, S.; Kojima, T.; Fukuzumi, S. *J. Am. Chem. Soc.* **2008**, *130*, 1556−1557.

DOI: 10.1021/ic502807d
Inorg. Chem. 2015, 54, 4621−4635

(8) For selected examples see: (a) Weisser, F.; Hohloch, S.; Plebst, S.; Schweinfurth, D.; Sarkar, B. *Chem.—Eur. J.* **2014**, *20*, 781. (b) Schweinfurth, D.; Weisser, F.; Bubrin, D.; Bogani, L.; Sarkar, B. *Inorg. Chem.* **2011**, *50*, 6114. (c) Schweinfurth, D.; Demeshko, S.; Khusniyarov, M. M.; Dechert, S.; Gurram, V.; Buchmeiser, M. R.; Meyer, F.; Sarkar, B. *Inorg. Chem.* **2012**, *51*, 7592. (d) Schweinfurth, D.; Krzystek, J.; Schapiro, I.; Demeshko, S.; Klein, J.; Telser, J.; Ozarowski, A.; Su, C.-Y.; Meyer, F.; Atanasov, M.; Neese, F.; Sarkar, B. *Inorg. Chem.* **2013**, *52*, 6880. (e) Schweinfurth, D.; Klein, J.; Hohloch, S.; Dechert, S.; Demeshko, S.; Meyer, F.; Sarkar, B. *Dalton Trans.* **2013**, *42*, 6944. (f) Donnelly, P. S.; Zanatta, S. D.; Zammit, S. C.; White, J. M.; Williams, S. J. *Chem. Commun.* **2008**, 2459. (g) Schweinfurth, D.; Demeshko, S.; Hohloch, S.; Steinmetz, M.; Brandenburg, J. G.; Dechert, S.; Meyer, F.; Grimme, S.; Sarkar, B. *Inorg. Chem.* **2014**, *53*, 8203. (h) Connell, T. U.; Schieber, C.; Silvestri, I. P.; White, J. M.; Williams, S. P.; Donnelly, P. S. *Inorg. Chem.* **2014**, *53*, 6503. (i) Crowley, J. D.; McMorran, D. In *Topics in Heterocyclic Chemistry*; Kosrmlj, J., Ed.; Springer: Berlin, 2012; Vol. *22*, pp 31. (j) Schulze, B.; Schubert, U. S. *Chem. Soc. Rev.* **2014**, *43*, 2522. (k) Schweinfurth, D.; Weisser, F.; Deibel, N.; Sarkar, B. *Nachr. Chem.* **2011**, *59*, 937. (l) Guha, P. M.; Phan, H.; Kinyon, J. S.; Brotherton, W. S.; Sreenath, K.; Simmons, J. T.; Wang, Z.; Clark, R. J.; Dalal, N. S.; Shatruk, M.; Zhu, L. *Inorg. Chem.* **2012**, *51*, 3465. (m) Ségaud, N.; Rebilly, J.-N.; Sénéchal-David, K.; Guillot, R.; Billon, L.; Baltaze, J.-P.; Farjon, J.; Reinaud, O.; Banse, F. *Inorg. Chem.* **2013**, *52*, 691.

(9) Toyama, M.; Inoue, K.; Iwamatsu, S.; Nagao, N. *Bull. Chem. Soc. Jpn.* **2006**, *79*, 1525.

(10) (a) Abboud, J.-L. M.; Foces-Foces, C.; Notario, R.; Trifonov, R. E.; Volovodenko, A. P.; Ostrovskii, V. A.; Alkorta, I.; Elguero, J. *Eur. J. Org. Chem.* **2001**, 3013−3024. (b) Schulze, B.; Escudero, D.; Friebe, C.; Siebert, R.; Görls, H.; Sinn, S.; Thomas, M.; Mai, S.; Popp, J.; Dietzek, B.; González, L.; Schubert, U. S. *Chem.—Eur. J.* **2012**, *18*, 4010−4025. (c) Ségaud, N.; Rebilly, J.-N.; Sénéchal-David, K.; Guillot, R.; Billon, L.; Baltaze, J.-P.; Farjon, J.; Reinaud, O.; Banse, F. *Inorg. Chem.* **2013**, *52*, 691−700. (d) Suijkerbuijk, B. M. J. M.; Aerts, B. N. H.; Dijkstra, H. P.; Lutz, M.; Spek, A. L.; van Koten, G.; Klein Gebbink, R. J. M. *Dalton Trans.* **2007**, 1273−1276.

(11) (a) Heath, G. A.; Yellowlees, L. Y. *J. Chem. Soc., Chem. Commun.* **1981**, 287. (b) Petroni, A.; Slep, L. D.; Etchenique, R. *Inorg. Chem.* **2008**, *47*, 951.

(12) (a) Welby, C. E.; Armitage, G. K.; Bartley, H.; Wilkinson, A.; Sinopoli, A.; Uppal, B. S.; Rice, C. R.; Elliott, P. I. P. *Chem.—Eur. J.* **2014**, *20*, 8467. (b) Welby, C. E.; Rice, C. R.; Elliott, P. I. P. *Angew. Chem., Int. Ed.* **2013**, *52*, 10826.

(13) (a) Wang, R.; Vos, J. G.; Schmehl, R. H.; Hage, R. *J. Am. Chem. Soc.* **1992**, *114*, 1964−1970. (b) Hage, R.; Haasnoot, J. G.; Reedijk, J.; Wang, R.; Ryan, E. M.; Vos, J. G.; Spek, A. L.; Duisenberg, A. J. M. *Inorg. Chim. Acta* **1990**, *174*, 77−85.

(14) (a) Muckerman, J. T.; Kowalczyk, M.; Badiei, Y. M.; Polyansky, D. E.; Concepcion, J. J.; Zong, R.; Thummel, R. P.; Fujita, E. *Inorg. Chem.* **2014**, *53*, 6904−6913. (b) Duan, L.; Fischer, A.; Xu, Y.; Sun, L. *J. Am. Chem. Soc.* **2009**, *131*, 10397−10399. (c) Mattson, B. M.; Pignolet, L. H. *Inorg. Chem.* **1977**, *16*, 488−491.

(15) (a) Montalti, M.; Credi, A.; Prodi, L.; Gandolfi, M. T. *Handbook of Photochemistry*, 3rd ed.; CRC Press: Boca Raton, FL, 2006; pp 601−604. (b) Hatchard, C. G.; Parker, C. A. *Proc. R. Soc. London, Ser. A* **1956**, *235*, 518−536. (c) Kuhn, H. J.; Braslavsky, S. E.; Schmidt, R. *Pure Appl. Chem.* **1989**, *61*, 187−210.

(16) Lever, A. B. P. *Inorg. Chem.* **1990**, *29*, 1271−1285.

(17) (a) Nicholson, R. S.; Shain, I. *Anal. Chem.* **1964**, *36*, 706−723. (b) Chou, M.; Creutz, C.; Sutin, M. *J. Am. Chem. Soc.* **1977**, *99*, 5615−5623. (c) Toma, H. E.; Rocha, R. C. *Croat. Chem. Acta* **2001**, *74*, 499−528. (d) Toma, H. E.; Araki, K. *J. Coord. Chem.* **1991**, *24*, 1−8. (e) Silva, D. O.; Toma, H. E. *Can. J. Chem.* **1994**, *72*, 1705−1708.

(18) Krejcik, M.; Danek, M.; Hartl, F. *J. Electroanal. Chem.* **1991**, *317*, 179.

(19) Sharma, R.; Knoll, J. D.; Martin, P. D.; Podgorski, I.; Turro, C.; Kodanko, J. J. *Inorg. Chem.* **2014**, *53*, 3272.

(20) (a) Evans, I. P.; Spencer, A.; Wilkinson, G. *J. Chem. Soc., Dalton Trans.* **1973**, 204. (b) Toyama, M.; Inoue, K.; Iwamatsu, S.; Nagao, N. *Bull. Chem. Soc. Jpn.* **2006**, *79*, 1525. (c) Ward, A. L.; Elbaz, L.; Kerr, J. B.; Arnold, J. *Inorg. Chem.* **2012**, *51*, 4694. (d) Chan, T. R.; Hilgraf, R.; Sharpless, K. B.; Fokin, V. V. *Org. Lett.* **2004**, *6*, 2853. (e) Hohloch, S.; Su, C.-Y.; Sarkar, B. *Eur. J. Inorg. Chem.* **2011**, 3067. (f) Fletcher, J. T.; Bumgarner, B. J.; Engels, N. D.; Skoglund, D. A. *Organometallics* **2008**, *27*, 5430.

(21) Sheldrick, G. M. *SHELX-97, Program for Crystal Structure Refinement*; University of Göttingen: Göttingen, Germany, 1997.

(22) (a) Neese, F. *ORCA—An Ab Initio, Density Functional and Semiempirical Program Package*, version 3.0.0; Department of molecular theory and spectroscopy, Max Planck Institute for Bioinorganic Chemistry, Mülheim/Ruhr, Germany, January 2012. (b) Becke, A. D. *J. Chem. Phys.* **1993**, *98*, 5648. (c) Lee, C. T.; Yang, W. T.; Parr, R. G. *Phys. Rev. B* **1988**, *37*, 785. (d) van Wüllen, C. *J. Chem. Phys.* **1998**, *109*, 392. (e) Weigend, F.; Ahlrichs, R. *Phys. Chem. Chem. Phys.* **2005**, *7*, 3297. (f) Baerends, E. J.; Ellis, D. E.; Ros, P. *Chem. Phys.* **1973**, *2*, 41. (g) Dunlap, B. I.; Connolly, J. W. D.; Sabin, J. R. *J. Chem. Phys.* **1979**, *71*, 3396. (h) Vahtras, O.; Almlof, J.; Feyereisen, M. W. *Chem. Phys. Lett.* **1993**, *213*, 514. (i) Eichkorn, K.; Greutler, O. T.; Ohm, H.; Haser, M.; Ahlrichs, R. *Chem. Phys. Lett.* **1995**, *242*, 652. (j) Eichkorn, K.; Weigend, F.; Treutler, O.; Ahlreichs, R. *Theor. Chem. Acc.* **1997**, *97*, 119. (k) Löwdin, P. O. *J. Chem. Phys.* **1950**, *18*, 365. (l) Löwdin, P. O. *Adv. Quantum Chem.* **1970**, *5*, 185.

DOI: 10.1021/ic502807d
Inorg. Chem. 2015, 54, 4621−4635